Numerical prediction of aeolian erosion on tandem sand piles using LES turbulence modes

Submitted in Partial Fulfilment of the Requirements for the Degree of Master in Mechanical Engineering in the speciality of Energy and Environment

Simulação computacional da erosão eólica em dunas sinusoidais usando modelos de turbulência do tipo LES

Author
Pedro Miguel Martins Brito

Advisor
Prof. **Almerindo Domingues Ferreira**

Jury

President	**Professor Doutor Pedro de Figueiredo Vieira Carvalheira** Professor Auxiliar da Universidade de Coimbra
Vowel	**Professor Doutor António Manuel Gameiro Lopes** Professor Auxiliar da Universidade de Coimbra
Advisor	**Professor Doutor Almerindo Domingues Ferreira** Professor Auxiliar da Universidade de Coimbra

Coimbra, July, 2019

To my family.

Acknowledgements

I would like to express my deepest gratitude to my scientific advisor, who provided crucial scientific guidance during the elaboration of this study. I truly thank Professor Almerindo Ferreira for all the time invested and his generous and frequent encouragements. Moreover, I must thank for the academic challenges proposed, whose completion added to my curriculum and stimulated my interest in contributing to the scientific community.

I would like to thank my parents, for their unconditional care throughout the last five years, during the course of my M.Sc. degree at the Department of Mechanical Engineering of the University of Coimbra.

My brother João supported me throughout the course, always encouraging me to be the best student I could be, so I am grateful for him. Also, I would like to recognize my friends and fellow colleagues, who I had the fortune to meet during the past years.

Abstract

Some CFD simulation results are presented on the triggering of wind-driven particle migration phenomena from a surface, so-called aeolian erosion, and the correspondent onset locations, from a pair of transverse sand piles in closely spaced tandem arrangement, of original sinusoidal outline and orthogonally placed in relation to the undisturbed incoming airflow.

Wind-tunnel experimental measurements (Ferreira and Fino, 2012), revealed that, contrary to expectations, the upstream pile remained virtually unchanged, while the downstream pile was considerably eroded over time. As the wall shear stress (WSS) is of prime importance when describing the wind erosion phenomena, its longitudinal distribution is experimentally probed in Ferreira et al. (2013), also for benchmarking numerical results.

In short, the onset of aeolian particle removal and transport from a solid surface occurs when the local threshold friction velocity ($u_{*\mathrm{t}}$) is exceeded. Howard (1977) suggests an $u_{*\mathrm{t}}$ expression for arbitrarily oriented surfaces. An adaptation of such formula is proposed to comply with the near-surface flow reversion induced by the sizable recirculation bubble formed in the interdune region, termed here "apparent friction velocity threshold" ($u_{*\mathrm{at}}$).

By means of a LES (Large Eddy Simulation) approach, bursts of activity are detected, *i.e.* localized and intermittent fluctuations of the u_*. The results of the LES are in agreement with the experimental observations and measurements of Ferreira and Fino (2012) and Ferreira et al. (2013). On the other hand, the RANS (Reynolds-averaged Navier-Stokes) numerical results evidence an inadequacy to forecast the manifestation of wind erosion as observed in the wind-tunnel experiments, although reliably predicting the time-averaged WSS distribution.

Keywords: CFD, Aeolian erosion, Apparent Threshold, Friction velocity, Interdune recirculation, Burst activity, LES.

Resumo

São expostos resultados de simulações CFD acerca do desencadeamento de fenómenos de migração de partículas de uma superfície por ação do vento, a chamada erosão eólica, e identificados os correspondentes locais de iniciação, a partir de um par de dunas (ou pilhas de areia) transversais, numa configuração em tandem não intervalada, de perfil inicialmente sinusoidal e colocadas perpendicularmente em relação ao escoamento de ar não perturbado.

As medições experimentais em túnel de vento (Ferreira and Fino, 2012) demonstram que, ao contrário das expectativas, a pilha a montante mantem-se praticamente inalterada, enquanto que a pilha a jusante é consideravelmente e sucessivamente erodida. Ainda, como a tensão de atrito parietal (WSS) governa a ocorrência de erosão eólica, a respetiva distribuição longitudinal foi avaliada experimentalmente no trabalho de Ferreira et al. (2013), também para servir de referência para os resultados numéricos análogos.

Em suma, a iniciação do destacamento eólico de uma partícula a partir de uma superfície sólida ocorre quando a velocidade de atrito (u_*) supera o limiar de velocidade de atrito local ($u_{*\mathrm{t}}$). Howard (1977) sugere uma expressão para $u_{*\mathrm{t}}$ válida para superfícies arbitrariamente orientadas. Uma adaptação dessa fórmula é proposta de modo a conformar com a reversão do sentido do escoamento na imediação das paredes, sentida na região entre as dunas e induzida pela larga zona de recirculação formada. Essa curva é designada no presente documento como "limiar de velocidade de atrito aparente" ($u_{*\mathrm{at}}$).

Por meio de uma simulação do tipo LES (Large Eddy Simulation), o fenómeno de rajada é detetado, que consiste fundamentalmente em flutuações localizadas e intermitentes de u_*. Os resultados dessa simulação genericamente concordam com as observações e medições experimentais de Ferreira and Fino (2012) e de Ferreira et al. (2013). Por outro lado, os resultados da simulação RANS (Reynolds-averaged Navier-Stokes) mostram inaptidão para prever a manifestação de erosão eólica tal como observado em túnel de vento, embora a distribuição média de WSS se ajuste bem com os pontos experimentais.

Palavras-chave: CFD, Erosão eólica, Limiar aparente, Velocidade de atrito, Recirculação entre dunas, Fenómeno de rajada, LES.

Contents

List of Figures

List of Tables

List of Symbols and Acronyms

Symbols

α	Velocity profile power-law exponent
α_{ls}	Angle of the slope on the dune lee side
α_r	Angle of repose
β_1	Wilcox ω_{wall} model constant
β^*	Menter ω_0 model constant
δ	Boundary layer thickness
δ_0	Grid spacing at zero-level refinement
δ_{ij}	Kronecker delta tensor
Δ	Characteristic cut-off scale or filter width
ε	Turbulent kinetic energy dissipation rate
ε_1	Relative error on the fine grid
η	Kolmogorov dissipation length scale
θ	Angle described by the slope in relation to the horizontal
λ	Spectroscopic wave-length
μ	Molecular dynamic viscosity
ν	Molecular kinematic viscosity
ν_t	Boussinesq eddy-viscosity
ν_t^{sgs}	Sub-grid scale eddy-viscosity
$\tilde{\nu}$	Spectroscopic wave-number
ρ	Air density
ρ_s	Sand grain (quartz) density
υ	Kolmogorov velocity scale
τ	Kolmogorov time scale

τ_w	Wall shear stress magnitude
τ_{ij}	Sub-grid scale stress tensor
ϕ	Generic scalar variable
$\bar{\phi}$	Time-averaged component of ϕ
$\tilde{\phi}$	Resolved (filtered) component of ϕ
ϕ'	Instantaneous deviation from $\bar{\phi}$ or unresolved component of ϕ
ω	Specific dissipation rate of turbulence kinetic energy
ω_0	Freestream value of ω
ω_{wall}	Near-wall value of ω

A	Dimensionless threshold friction velocity
C_f	Skin friction coefficient
C_{ij}	Cross term tensor
Co	Courant number
d	Particle prevailing diameter
D	Interdune spacing
E_1	Normalized discretization error in the fine grid
f	Simulated quantity value
f_1	Simulated quantity value on the finer grid
f_2	Simulated quantity value on the medium grid
f_3	Simulated quantity value on the coarser grid
$f_{h=0}$	Simulated quantity at zero grid spacing
F_s	Safety factor
g	Gravitational acceleration modulus
G	Filtering kernel of the convolution
GCI_{fine}	GCI evaluated between the medium and finer grids
GCI_{2-3}	GCI evaluated between the coarse and medium grids
H	Original dune height

I	Turbulent intensity number
k	Turbulence kinetic energy
k_0	Freestream value of k
k_{wall}	Near-wall value of k
l	Eddy length scale
l_0	Integral scale
l_{r}	Recirculation zone length
L	Streamwise dune length
L_{ij}	Leonard term tensor
N_{y}	Number of cells in the transverse direction
N_{total}	Total number of cells in the grid
p	Order of convergence rate
$\bar{p}$	Time-averaged pressure
$\bar{p}_{\text{m}}$	Time-averaged modified pressure
$\tilde{p}_{\text{m}}$	Resolved modified pressure
Re_H	Reynolds number based on the dune height
Re_{K41}	Kolmogorov Reynolds number
$Re_{u_{*_t}}$	Reynolds number at the threshold friction velocity
R_{ij}	Reynolds stress tensor
S_{ij}	Mean strain rate tensor
S_{ij}^{*}	Traceless mean strain rate tensor
$\tilde{S}_{ij}$	Filtered strain rate tensor
t_1	Fluctuating field time scale
Δt	Time interval considerably larger than t_1
Δt_{exec}	Total execution time of the simulation
Δt_{s}	Time step of the simulation
u	Longitudinal mean velocity component

u_*	Friction velocity
$u_{*\text{t}}$	Threshold friction velocity
$u_{*0\text{t}}$	Threshold friction velocity for horizontal surfaces
$u_{*\text{t}\theta}$	Threshold friction velocity for inclined surfaces
$u_{*\text{at}}$	Apparent threshold friction velocity
u_*^{bounded}	Bounded time-averaged friction velocity
$\bar{u}_i$	Time-averaged velocity component in the i direction
$u_i^{'}$	Velocity fluctuation around the $\bar{u}_i$ value
U_0	Undisturbed airflow velocity
y^+	Dimensionless distance from wall to first cell-centre
Δy_1	Distance to first cell-centre

Acronyms

3D	Three-Dimensional
ADAI	Associação para o Desenvolvimento da Aerodinâmica Industrial
CAD	Computed Aided Design
CAE	Computed Aided Engineering
CFD	Computational Fluid Dynamics
CFL	Courant-Friedrichs-Lewy condition or Courant Number
DES	Detached Eddy Simulation
DNS	Direct Numerical Simulation
FEA	Finite Element Analysis
FOAM	Field Operation and Manipulation
FVM	Finite Volume Method
GCI	Grid Convergence Index
HVAC	Heating, Ventilation and Air Conditioning
ILES	Implicit Large Eddy Simulation
LAI	Laboratório de Aerodinâmica Industrial
LES	Large Eddy Simulation
LIC	Line Integral Convolution
LPF	Low-Pass Filter
NACA	National Advisory Committee for Aeronautics
NPARC	National Program for Applications-Oriented Research in CFD
OS	Operating System
PISO	Pressure-Implicit with Splitting of Operators
RAS	Reynolds-averaged Simulation
RANS	Reynolds-averaged Navier-Stokes
SIMPLE	Semi-Implicit Method for Pressure Linked Equations
SGS	Sub-grid Scale

SST	Shear Stress Transport
STL	Stereolithographic
TKE	Turbulence Kinetic Energy
URANS	Unsteady Reynolds-averaged Navier-Stokes
VLES	Very Large Eddy Simulation
WALE	Wall-adapting Local Eddy-viscosity
WSS	Wall Shear Stress

1. Introduction

This chapter presents the motivation for the work and a brief description of Computational Fluid Dynamics (CFD) as an important design tool in numerous engineering domains. The primary objectives of the thesis, as well as the structure and content of the document, are also presented.

1.1. Motivation

Among a wide range of topics, wind engineering deals with the aerodynamic study of sand dunes, namely the triggering of wind-driven particle migration, a phenomenon so-called aeolian erosion. Once erosion is triggered, sand particles are transported by the incoming wind and some negative environmental impacts may occur, such as poor air quality and adverse conditions for plant pollination in the affected areas, to name a few (Faria et al. 2011). The interaction of these particles with human infrastructures in arid environments, as well as the loss of disaggregated material in an industrial environment or during cargo transport, are other examples that motivate the experimental and numerical study of the sand dune dynamics, encompassing the wind ability to induce erosion.

1.2. The relevance of CFD

Computational Fluid Dynamics is a relatively recent Computer Aided Engineering (CAE) tool, nowadays at a level of technical viability and industrial-endorsement parallel to those of the Finite Element Analysis (FEA) for Solid Mechanics and Vibration.

In the early 1990s, little over two decades since the development of the SIMPLE algorithm by Patankar and Spalding (1972), CFD was already seen as a third branch of the scientific method, accompanying the experimental development and mathematical theory as an engineering tool for research and development (Moukalled et al., 2016). Anderson and Wendt (1995) argue that CFD synergistically complements the theoretical and experimental approaches and will never replace either of them, also underlining the portability of a CFD code, designating it a "*transportable wind-tunnel*".

Even though the impetus to its development is originally provided by some challenges faced by the aeronautic and aerospace industries, it has matured to become an essential, mainstream tool in a range of other design-intensive industries, such as automotive, chemical and marine, to name a few. More recently, other industries have employed CFD evaluations, as in the electronic industry (*e.g.* optimizing heat transfer for the cooling of electronic devices), biomedical engineering (*e.g.* simulation blood flow on arteries), HVAC and fire simulation (Moukalled et al., 2016).

Besides the technical restrictions on computing and data storing, the reason for the delayed establishment of CFD is the complexity of the governing equations to be solved, that is, the Navier-Stokes equations (Navier, 1823; Stokes, 1845), primarily refereed to the conservation of linear momentum and sometimes used to collectively denote the conservation of mass, momentum and energy. This differential equation system, amazingly enough, accurately models a whole set of flow phenomena, from laminar to turbulent, single or multiphase, compressible or incompressible flows.

A numerical technique commonly implemented in CFD is the Finite Volume Method (FVM), which transforms the governing, partial differential equations of the fluid flow into discrete, algebraic equations over non-overlapping finite volumes, which form a structured computational grid (or mesh). The mentioned transformation is performed by discretization, *i.e.* integrating the partial differential equations over each discrete element. Because the flux entering a given volume is identical to that leaving the adjacent, the FVM is strictly conservative (even at unstructured polygonal meshes), thus the preferred numerical method in CFD (Moukalled et al., 2016). The performed simulations are conducted on OpenFOAM® v6 (Open Field Operation and Manipulation, version 6), an open-source, finite volume code which is comprised of a collection of libraries written in C++ language (OpenFOAM Foundation Ltd., 2018).

1.3. Objectives of the work

The numerical prediction of aeolian erosion in transverse sand dunes is a subject already attended in papers such as Faria et al. (2011), Ferreira et al. (2013), and Ferreira et al. (2018). The present study aims to complement the formers, responding to some of its challenges and, at its conclusion, opening up new ones for further investigation on the topic. One can summarize the prime objectives as listed below.

i. Generate a high-quality mesh using the OpenFOAM®-supplied utilities.

ii. Based on the literature review, select a turbulence model suitable for the case.

iii. Attain CFD simulation results that indisputably suggest the occurrence of wind erosion as experimentally observed in the wind-tunnel measurements of Ferreira and Fino (2012).

iv. Enunciate a mathematical correlation for the variable that controls the initiation of aeolian particle removal (*i.e.* threshold curve), considering the prescribed dune geometry and local flow topology. The completion of this objective is crucial for the closure of the above and the following.

v. Perform a grid refinement study to authenticate the numerical results.

vi. Study and confront the aptitude of the different turbulence treating numerical approaches to describe the onset of aeolian erosion, namely the RANS (Reynolds-averaged Navier-Stokes), the LES (Large Eddy Simulation) and DES (Detached Eddy Simulation) methods.

1.4. Layout of the thesis

The content of the dissertation is comprised of five chapters that may be grouped in two main parts. The first part includes Chapter 2 and Chapter 3 and is mostly a literature review, providing the necessary background for introducing the simulation results. The review is by no means detailed, but it is inclusive. Also, the aforementioned fourth objective is dealt. The second part coincides with the broad Chapter 4, where the remaining objectives of the work are covered. The respective contents can be condensed as follow.

In Chapter 2 some foremost comments are drawn in regard to the theory of aeolian erosion, *e.g.* a reference on transverse dune geomorphology and the main aeolian particle transportation mechanisms. The case study and experimental measurements are elucidated. Also, the concept of erosion threshold curve is introduced and reformulated.

In Chapter 3 an overview on turbulence modelling is presented, including some prime remarks about turbulence itself, followed by a succinct description on the different numeric turbulence treating approaches currently available in CFD commercial codes. This literature review provides an academic support for the following discussion of the simulation results.

In Chapter 4 the numerical setup and numeric results are revealed and discussed. Concerning the numerical setup, some insight is presented in regard to the used discretization

schemes, convergence criteria and the generated computational grid(s). Also, some comments are established about the intended selection of the SST k-ω model (Menter et al., 2003), namely its aptitude for the problem at hand and the respective boundary conditions. Regarding the numerical results, the simulated solutions are disclosed and compared with experimental data. Also, a grid convergence study is performed and the numerical solutions for dissimilar turbulence models confronted.

In Chapter 5 is presented a short synopsis of the issues addressed in the study and the main conclusions withdrawn from it, along with suggestions for future research.

2. The wind erosion phenomena in sand dunes

This chapter provides an overview of the fundamental concepts and formulates a mathematical description of the aeolian erosion mechanisms. Following the literature review on transverse dune geomorphology and characteristic flow topology, the studied geometry and inflow conditions are described. The chapter ends with a summary of the applicable friction velocity threshold equations and an adaptation for present case.

2.1. Remarks on transverse dune geomorphology and flow topology

In locations with an abundance of sand and where the incident wind is orientated towards a dominant direction, the transverse dunes - those with a nearly fixed profile in the direction perpendicular to the first - are the predominant dune, or pile, type (Bruno and Fransos, 2015). Transverse dunes have an idealized cross-section and geomorphic terminology, as represented in Figure 2.1. Firstly, these structures possess a ridge crest. The lee side, or leeward slope, is located downwind of the crest, and the windward side, or stoss slope, is upwind from the crest. The slope angle at which sand begins to naturally avalanche is termed the angle of yield and the angle at which avalanching sand comes to rest is the angle of repose. Per definition, the slip face is a sub-region of the pile in the lee side, where the slope is near the latter angle. A brink can be found, which divides the top of the dune from its inclined slip face. The area between two contiguous transverse piles is called interdune region, often flat and erosion-resistant, and a pair of dunes with this configuration is said to be in tandem (Elder, 2006).

Because their replicable geometry and frequent occurrence in deserted regions, transverse sand piles are usually adopted in the literature as benchmark to investigate about fundamental dune aerodynamics, both computationally and experimentally, in bidimensional formats. Furthermore, ideal crested dunes (*i.e.* no brink, or crest-brink separation, can be identified) are regularly implemented, to further simplify the configuration (Bruno and Fransos, 2015).
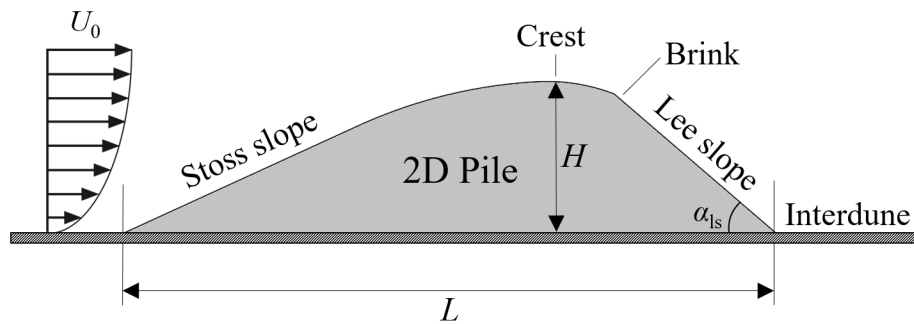
Figure 2.1. Cross-section of a typical transverse dune and respective terminology.

In terms of aerodynamic behaviour and flow topology, a single transverse sand pile with a sufficiently steep lee slope (α_{ls}), (Finnigan (1988) and Sweet and Kocurek (1990) propose the critical values of 16º and 20º, respectively), when exposed to an orthogonal incident flow, can be classified as a bluff body (Bruno and Fransos, 2015). Under appropriate conditions, this structures typically present separation of the boundary layer just downwind the crest line, with the reattachment occurring far downstream of the dune leeward toe, extending over several times the dune height. As far as tandem piles are concerned, in identical environments, a considerable recirculation bubble may be found in the interdune region, as well as a second, albeit significantly shorter than the first, in the lee side of the downwind dune (Schatz and Herrmann, 2006). The extent of these recirculation zones (l_R), as the corresponding reattachment locations, are highly sensitive to several parameters like the Reynolds number, surface roughness and incoming turbulence (Bruno and Fransos 2015), being also dependent on geometric characteristics of the dunes, particularly the height of the crest (H) and the shape at the slip face (Herrmann et al., 2005). In Figure 2.2 the described aerodynamic behavior is schematically illustrated for both single and tandem arrangements.

When a transverse sand dune with a certain initial silhouette is subjected to aeolian erosion, a complex morphological time-dependent evolution of its contour is observed, which is governed by a set of physical processes that act simultaneously and can be interdependent, such as the airflow features (*e.g.* regime and direction), local topography changes and the active sediment transport mechanisms (Ferreira et al., 2013). This deformation of the initial outline into an asymmetrical pile, generally with a slip face in the lee, occurs for dunes with relatively steep gradients on the slopes as described by Bagnold (1941).
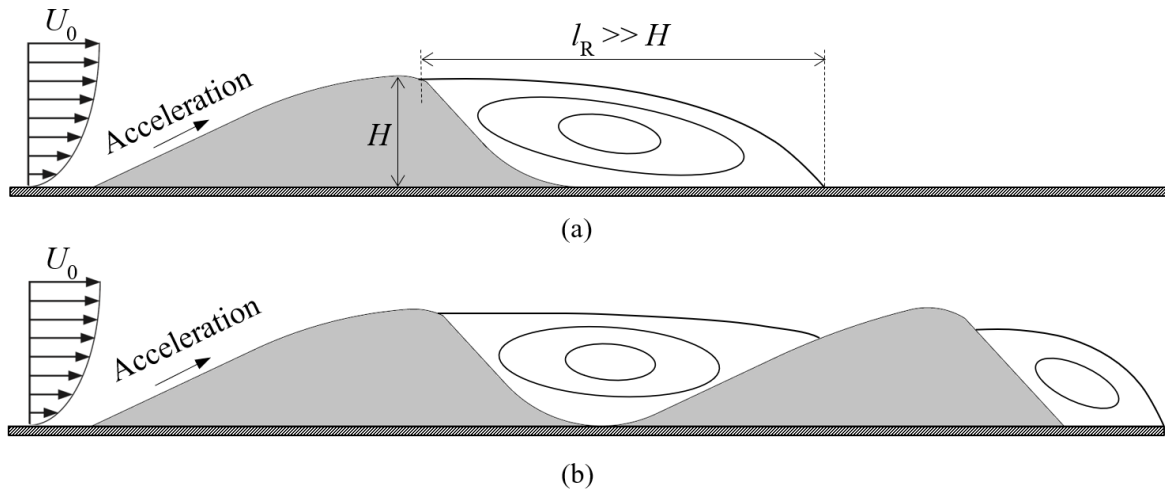
Figure 2.2. Descriptive scheme of the flow topology over: (a) single pile; (b) tandem piles.

The abovementioned particle transport processes by wind erosion are categorized in three main mechanisms (National Soil Erosion Research Laboratory - NSERL, 2009). On a ground surface these can coexist, but depending on the prevailing particle size, one can stand out from the others. Large diameter particles (larger than 0.5 mm) are hauled and rolled by drag forces over the solid surface without abandoning it, a process known as *creeping*. On the other hand, *saltation* is the transport mechanism where the particles involved are among 0.1 and 0.5 mm in diameter. The aerodynamic lift forces can briefly lift them, and advection occurs for short time intervals, before being released in the granular bed. As the particles collide with the surface, they exchange momentum with other grains, rebounding back into the airstream or ejecting them after collision. When saltation is the foremost process of aeolian erosion, a regime of intermittent flux characterized by bursts of activity can arise, as described by Carneiro et al. (2015). A burst can be seen as a sporadic, instantaneous fluctuation around the threshold controlling the initiation of sand movement, and despite being quite common, little is known about this intermittent phenomenon. Lastly, the *suspension* process is active for very small granulometry particles, like fine dirt and dust (less than 0.1 mm in diameter). Wind can sustain these particles airborne over very long distances and this mechanism is responsible for other phenomena such as surface abrasion.

Case intricacies, as well as the chaotic nature of the erosion processes, hamper the establishment of general-purpose models that predict particle entrainment and transport. Consequently, the experimental route, namely with the use of wind-tunnel testing, is fundamental to validate any attempt to model and forecast wind erosion phenomena on non-

cohesive sand particles laying on pile outlines, either theoretically or, as the purpose of the present document, computationally. Therefore, in the following subchapter it is summarized the work of Ferreira and Fino (2012) and Ferreira et al. (2013).

2.2. Case study and experimental results

Briefly, the work of Ferreira and Fino (2012) consisted in the experimental measuring, resorting to the wind-tunnel installed at the Industrial Aerodynamics Laboratory (LAI) of ADAI, of the time-evolving mean longitudinal profile of a set of two-dimensional transverse sand piles, single and placed in tandem, with the same initial height and a sinusoidal outline described by Equation (2.1), in which H is the original maximum height, and L is the streamwise length.

$$z = \frac{H}{2}\left[1+\sin\left(\pi\left\{\frac{2x}{L}+\frac{1}{2}\right\}\right)\right] \tag{2.1}$$

From the wide-ranging set of pile arrangements, aspect ratios and flow velocities tested and reported in the same paper, the over time profile reshaping for the closely spaced, tandem configuration illustrated in Figure 2.3, whose geometric details are briefed in Table 2.1, presented an unanticipated and interesting behaviour when the undisturbed wind speed in the test section, U_0, was 8.3 m/s (an incompressible air flow). In the next section, some insight is presented why this particular wind speed was tested. All the computational simulations performed, whose results are revealed in Chapter 4, focus on this precise configuration and prescribed conditions.

Table 2.1. Geometric characteristics of the tandem pile arrangement studied (Ferreira and Fino, 2012).

Variable	Symbol	Value
Initial crest height	H [mm]	60
Streamwise length	L [mm]	360
Original aspect ratio	(L/H)	6
Dune spacing	D [mm]	0
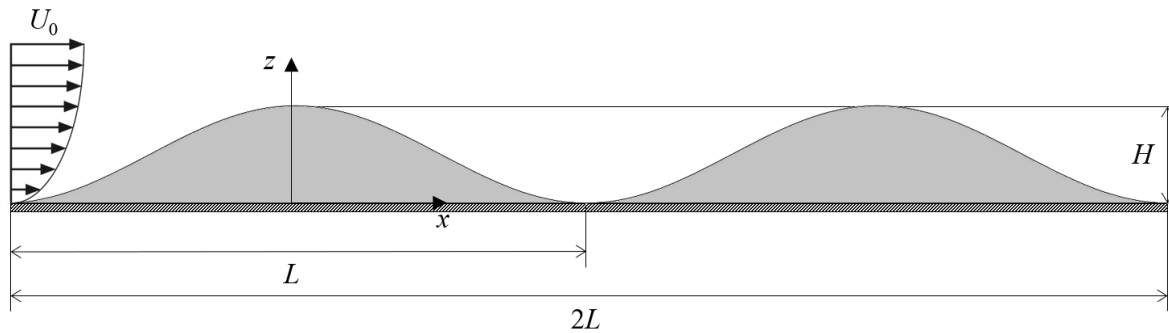
Figure 2.3. Closely spaced, tandem pile configuration studied in the present work.

Contrary to expectations, and incidentally, differing from observations for similar arrangements tested with slightly higher free-flow velocity (*e.g.* U_0=9.1 m/s), the measured contours showed that the upstream pile remained virtually unchanged, while the downstream pile was considerably eroded over time, as shown in Figure 2.4. A sheltering effect was foreseen from the first dune in relation the second, but that was not the case. Moreover, this behaviour greatly diverged from the negligible, over time erosion observed for a single homologous pile subjected to the same conditions, which effectively retained its original shape. At the time, the researchers attributed the described behaviour as a consequence of the establishment of an interdune recirculation zone, since the maximum slope in the lee side of the original profile of about 27.6 °, clearly exceeds the critical angles mentioned in the previous paragraph (Finnigan 1988; Sweet and Kocurek 1990), below witch stable separation in the dune leeward is achieved.
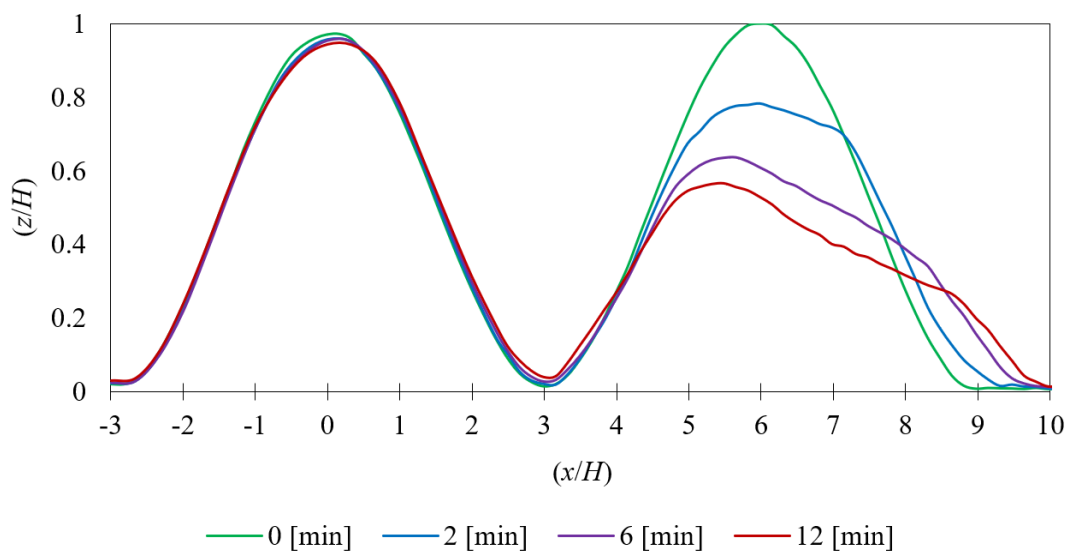
Figure 2.4. Mean eroded contours, at several time instants, presented in (Ferreira and Fino, 2012).

The crest of the upwind pile of the tandem arrangement studied was placed about mid-length of the wind tunnel working chamber span, which is about 5 m long, with a 2 m × 2 m cross-section. As Faria et al. (2011) and Ferreira et al. (2013) reason, such short test section precludes the use of mixing devices or roughness elements to thicken or control the boundary layer. The resulting fully developed boundary layer profile at the designated location, measured in the empty chamber at half-width, can be fitted by the power law described by Equation (2.2), where u is the longitudinal mean velocity component, U_0 the freestream wind velocity and z the vertical coordinate above the chamber base. The boundary layer thickness is gauged at δ=0.1 m, with the exponent α=0.11 (Faria et al. 2011; Ferreira et al. 2013). The turbulence intensity of the longitudinal velocity component remains nearly unchanged with the vertical coordinate and it is estimated to be equal to 10%.

$$\frac{u}{U_0} = \left(\frac{z}{\delta}\right)^{\alpha} \tag{2.2}$$

The Reynolds number based on the original crest height (Re_H) in the wind tunnel tests and, thus, numerical simulations, is evaluated at 3.32×10^4 for the free stream velocity of U_0=8.3 m/s. Consequently, being an external flow, turbulence is not fully developed. It is important to note that in real world scenarios the dunes length scales, and therefore the Re_H itself, might be several orders of magnitude greater than this value, and the flow is indisputably turbulent. As Ferreira and Fino (2012) argue, full-scale conditions are not flawlessly replicated in their wind tunnel experiments due to some similitude principles not being obeyed, but for Reynolds numbers (the most important dimensionless parameter in this flow category) greater than 10^4, as the case, it is appropriate to assume that Reynolds number independence has been reached, as proposed in White (1996).

The longitudinal wall shear stress (τ_w), or the friction velocity (u_*) distribution, which comprises identical information and is a function of the first as seen in Equation (2.3), is of primary importance to recognise soil erosion processes, as described by Iversen and Rasmussen (1994), among other authors. In short, the onset of aeolian particle removal and transport from a solid surface through saltation occurs when the local threshold friction velocity (u_{*t}) is exceeded, which has diverse formulations according to different authors (Carneiro et al. 2015). Therefore, it is crucial to experimentally gauge the friction velocity distribution along the prescribed tandem piles original profile, measurements which may be

confronted with the above-mentioned theoretical limits, thus predicting the manifestation and location of wind erosion phenomena along these structures. Also, the same distribution can serve as a benchmark to computationally assess the different CFD turbulence modelling approaches aptitude, or lack off, to compute the same quantities, through direct comparison between numerical and experimental results. For these reasons, in Ferreira et al. (2013) the wall shear stress longitudinal distribution is probed along single-placed and tandem, rigid piles, for similar arrangements and inflow conditions as described in Ferreira and Fino (2012), by means of a set of symmetrically mid-plane installed Irwin probes (Irwin, 1981). The measurements resort to sand roughened, aluminium sheets replicating the original tandem sand piles profile, illustrated in Figure 2.3. The measured friction velocity distribution is presented in Figure 2.5, for $Re_H = 3.32 \times 10^4$ (*i.e.* $U_0 = 8.3$ m/s), in a dimensionless format, through the equivalent wall friction coefficient, or skin friction coefficient (C_f), as defined in Equation (2.4).

$$u_* = \sqrt{\frac{\tau_w}{\rho}} \tag{2.3}$$

$$C_f = 2\left(\frac{u_*}{U_0}\right)^2 \tag{2.4}$$
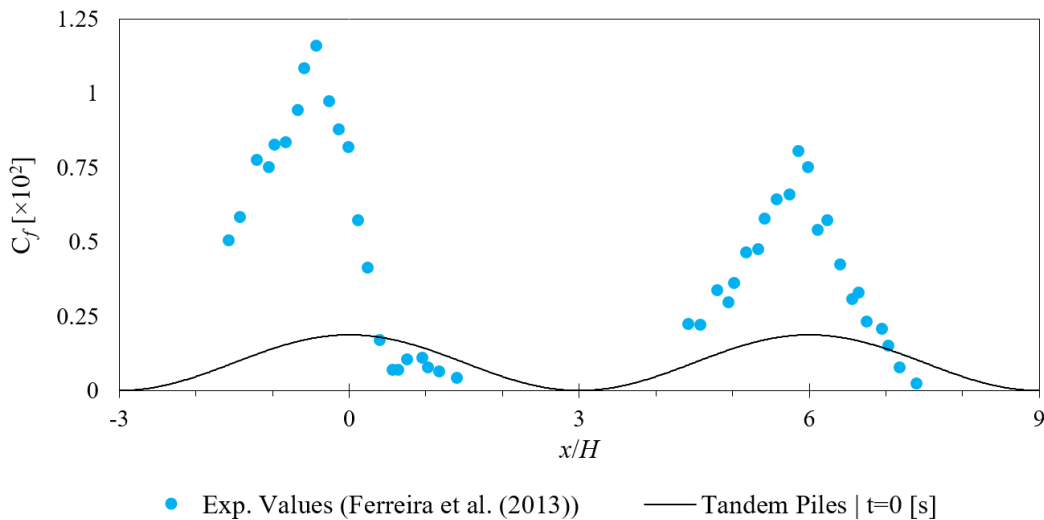
Figure 2.5. Probed C_f longitudinal distribution along the tandem dunes ($Re_H = 3.32 \times 10^4$).

2.3. The concept of threshold friction velocity

The threshold friction velocity (u_{*t}) represents the capacity of a granular surface to resist wind erosion, and although is affected by a range of factors such as soil texture, soil moisture, soil salt content, surface crust and roughness elements, under ideal conditions, it is a function only of the particle predominant size (Shao and Lu, 2000).

When loosely spread sand grains, idealized as uniform spherical and undeformable particles of a prevailing diameter, rest on a dry and bare surface subjected to an incoming airstream, different forces act upon them. The literature presents a set of more or less complex expressions for u_{*t}, all of them having their derivation based on the balance between the overturning moments induced on a single particle by the driving forces, namely the aerodynamic drag and lift, and the retarding forces, the particle weight and inter-particle cohesion forces (Bagnold, 1941; Greeley and Iversen, 1987; Phillips, 1980). The sole dependence of the threshold friction velocity expression on the particle diameter, valid for the described conditions, turns out to be a meaningful relation, since it defines the lowest u_{*t} limit for any given type of soil (Shao and Lu, 2000).

The simplest and most widely-used expression for u_{*t} is proposed by Bagnold (1941), shown in Equation (2.5), and it considers exclusively the balance between the aerodynamic drag and the gravity forces acting on cohesionless particles laying on a horizontal bed (subscript "0"). The demonstration of its derivation can be consulted in the Annex A.

$$u_{*t0} = A \times \sqrt{\frac{(\rho_s - \rho)}{\rho} \cdot d \cdot g} \qquad (2.5)$$

In the same equation, ρ_s is the sand grain density (comparable to quartz), ρ is the fluid density (air at standard sea-level conditions, in this case), g is the gravitational acceleration modulus and d is the prevailing particle diameter, whose values are summarized in Table 2.2.

Table 2.2. Input values for Bagnold´s equation, evaluated in Faria et al. (2011).

Variable	Symbol	Value
Quartz grain density	ρ_s [kg·m^{-3}]	2650
Air density (Standard sea-level)	ρ [kg·m^{-3}]	1.23
Prevailing particle diameter	d [μm]	500
Gravitational acceleration modulus	g [m·s^{-2}]	9.81

The variable A in Equation (2.5) is termed the dimensionless threshold friction velocity, or simply the "Bagnold´s threshold parameter". The value of A is dependent on the friction Reynolds number at the correspondent threshold friction velocity, *i.e.* $A=A(Re_{u*t})$. It has been found to be a constant between 0.1 and 0.2 for $Re_{u*t} > 3.5$ (Shao and Lu, 2000) and generally its value is not well-defined and needs to be adjusted case by case to comply with experimental observations.

As Iversen et al. (1976) argues, Equation (2.5) is valid only when applied to particles larger than 100 μm. In fact, amid $d\sim10^{-1}$ mm to $d\sim10^{1}$ mm, experimental data corroborates the proportionality of u_{*t} with $d^{1/2}$ proposed by Bagnold (1941), and further observations display a threshold minimum around $d=75$μm, with a rapid increase of u_{*t}, as the particle diameter further decreases, a behavior attributed to the magnification of the inter-cohesive forces (Greeley and Iversen, 1987; Iversen et al., 1976; Iversen and White, 1982). As the prevailing diameter of the sand composing the dunes in the experimental tests ($d=500$ μm) is well within the range of applicability of Equation (2.5), it is not necessary to resort to more complex formulations of u_{*t0}, such as those of Greeley and Iversen (1987) and Shao and Lu (2000), which also take into account the aerodynamic lift and inter-cohesive (*e.g.* van der Walls and electrostatic) forces. It is also important to emphasize that for $d=500$ μm, saltation is the main particle transport process, thus the abovementioned effects of burst activity are to be expected.

At this point it is appropriate to explain why the velocity of undisturbed flow (U_0) was set at 8.3 m/s. Experimental observations demonstrate that it is the minimum wind tunnel airstream speed above which the friction velocity (u_*) on a flat granular bed exceeds the corresponding Bagnold's threshold formula (with $A=0.11$), evaluated at $u_{*t0}=0.33$ m/s for the prescribed conditions summarized in Table 2.2 (Ferreira and Fino, 2012).

Howard (1977) suggests a generalization of the latter equation so that the concept of threshold friction velocity applies to arbitrarily oriented aeolian surfaces, which describe any angle (θ) with the horizontal plane. So, the opposition to the triggering of particle movement by wind erosion of loose grains resting on a tilted surface is governed by Equation (2.6). A new variable arises, the angle of repose (α_r), whose definition is stated in Section 2.1 and for which a value of 32º is commonly employed in the absence of interparticle forces (Ferreira and Fino, 2012). For clarity, the subscript "θ" is added to distinguish the Howard´s threshold from the formerly presented in Equation (2.5).

$$u_{*t\theta} = u_{*t0} \times \sqrt{\cos\theta + \frac{\sin\theta}{\tan\alpha_r}} \qquad (2.6)$$

It is interesting to note that, when applied to the closely spaced tandem piles, the friction velocity threshold ($u_{*t\theta}$) is, likewise, a sinusoidal function, and the two curves are out of phase in relation to one other, as it will we illustrated ahead. Naturally, lower shear stress is needed in a downhill slope to dislodge a sand grain, as the weight of the particle (F_g), at that point, is not opposing the movement, but driving it, assisting the aerodynamic drag (F_d), as schematically illustrated in Figure 2.6. The opposite is true in a uphill. Therefore, the theoretical maximum and minimum of $u_{*t\theta}$ occur when $|\theta|=27.6°$, for the present dune profile, at the stoss slope and at the lee slope, respectively, as seen in Figure 2.7.
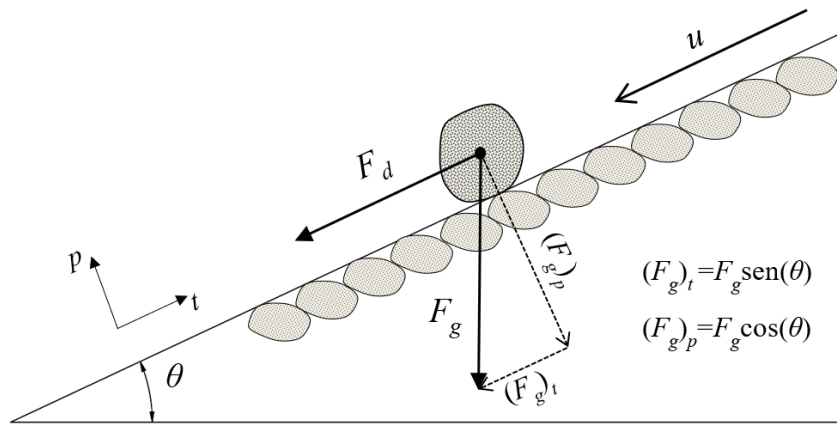
Figure 2.6. Driving forces acting on a particle resting in a downhill slope (absence of retarding forces).
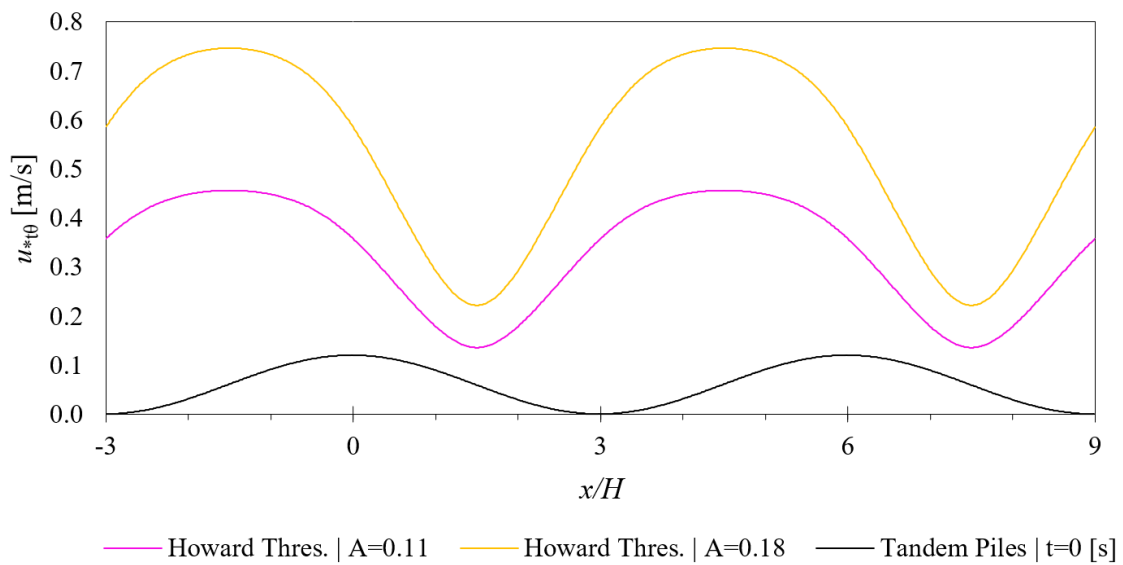
Figure 2.7. Theoretical Howard (1977) friction velocity threshold curves, applied to the tandem piles.

The theoretic $u_{*t\theta}$ distribution along the tandem piles outline presented in Figure 2.7 implicitly assumes that the direction of the airflow does not change, *i.e.* from upstream to downstream of the dune composition, in all its longitudinal extension, with the flow always remaining attached to the surface. With some insight (Ferreira et al., 2013) and as discussed in the first paragraphs, in truth, sizable recirculation zones appear along these structures, namely in the interdune region and in the lee of the second pile. An adaptation of the Howard´s formula (Howard, 1977) is then proposed to comply with the near surface flow reversion, termed here "apparent friction velocity threshold" (u_{*at}). The modification consists in employing the symmetrical θ angle within the recirculation areas and preserving its true sign where the boundary layer remains attached. Labelling $(x/H)_R^i$ as the coordinates that mark the mean position of the beginning ($i=1$) and ending ($i=2$) of the recirculation bubbles, Equation (2.7) mathematically describes u_{*at}. The reason why time-averaged positions are adopted is due to the spontaneous and chaotic character of the turbulent flow regime (and therefore, of the saltation mechanism itself), since the length of the recirculation zones actually fluctuates around a mean value, as the starting and ending positions retreat or advance instantly and independently along the dunes slopes. The described time-averaging approach is suitable for numerical CFD evaluation of the extent of those areas. In experimental methods, the visualization of wool turfs glued on the models and wind tunnel floor, complemented with seven-hole probe measurements, can provide benchmarks to compare with the computational flow topology results (Ferreira et al., 2013).

$$
u_{*at} = \begin{cases} u_{*t0} \times \sqrt{\cos\theta - \dfrac{\sin\theta}{\tan\alpha_r}} & \text{if } \dfrac{x}{H} \in \left[\left(\dfrac{x}{H}\right)_R^1, \left(\dfrac{x}{H}\right)_R^2 \right]_{\text{interdune/ lee dune}} \\[4mm] u_{*t0} \times \sqrt{\cos\theta + \dfrac{\sin\theta}{\tan\alpha_r}} & \text{if } \dfrac{x}{H} \notin \left[\left(\dfrac{x}{H}\right)_R^1, \left(\dfrac{x}{H}\right)_R^2 \right]_{\text{interdune/ lee dune}} \end{cases}
\tag{2.7}
$$

In Figure 2.8 the $u_{*t\theta}$ (Howard, 1977) and u_{*at} distributions are compared along the tandem piles in the form of the skin friction coefficient (C_f). The position of the separation points in the same illustration was assessed computationally. A key aspect to note from Figure 2.8 is that the newly proposed friction velocity threshold overlaps the customary Howard´s formula in the attached flow regions and mirrors it along the recirculation zones extent. Due to the occurrence of recirculation, the stoss slope of the downwind pile is,

contrarily to what was expected from Equation (2.6), the most susceptible site for the occurrence of aeolian erosion and, conversely, the lee slope of the upwind dune the least prone to be affected by the same phenomenon. Also, in the vicinity of the cross-marked points highlighted in Figure 2.8, the real threshold controlling the triggering of aeolian erosion randomly oscillates between the local $u_{*t\theta}$ and u_{*at} values.
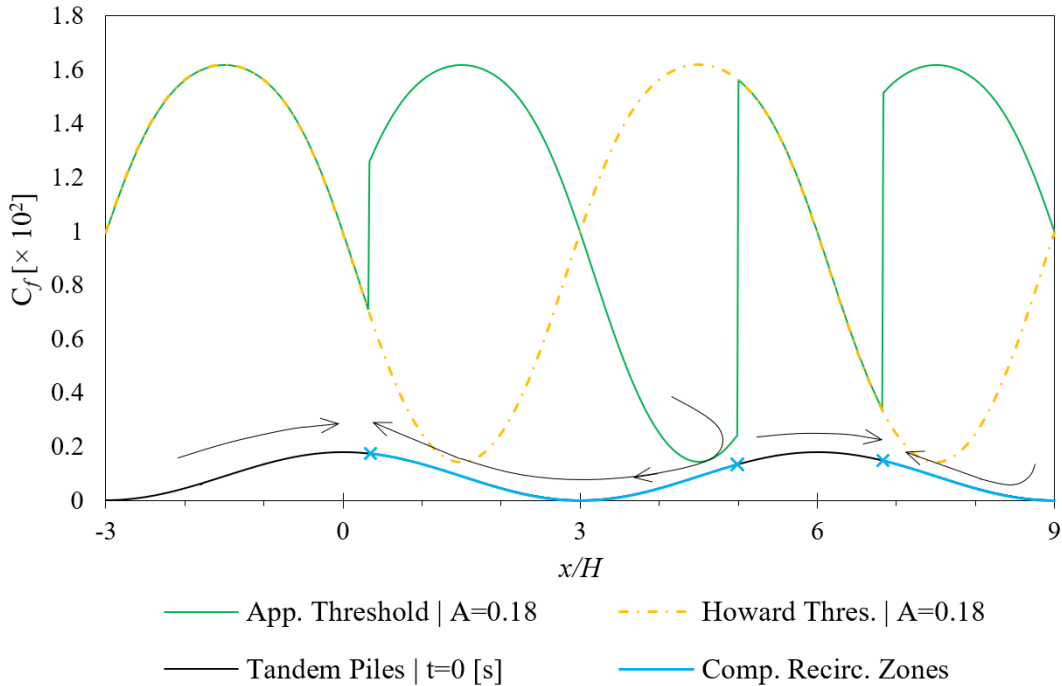
Figure 2.8. Comparation between threshold friction coefficient distribution along the tandem piles.

This is a foremost observation and a breakthrough to the problems described in Ferreira et al. (2013), where a RANS simulation seemingly failed to replicate the manifestation of erosion as observed experimentally in Ferreira and Fino (2012) when the classic threshold was implemented, presented in Figure 2.7. With some insight to the results of the analogous numerical simulation performed, presented in detail on Chapter 4, a RANS approach is, indeed, able to predict such behaviour (albeit with an appropriate turbulence model) if u_{*at} is instead adopted.

3. An introduction to turbulence modelling

The vast majority of the flows in engineering applications, as well as those found in natural environments, occur under turbulent regime. Therefore, one of the purposes of CFD simulations is to numerically model, up to an acceptable level of detail, the effects of turbulence, whose exact physical nature is not yet fully understood. For the purpose of introducing turbulence modelling in single-phase incompressible flows, some concepts and physical principals of this flow regime are firstly presented.

3.1. Some physical concepts regarding turbulence

A key aspect of turbulence is that is always three-dimensional (3D) and unsteady (Zhiyin, 2015). Another foremost property of turbulence is the existence of a continuous spectrum of scales, quantified by their spectroscopic wave-lengths (λ) or wave-numbers ($\tilde{\nu}$), with the largest scale being the integral scale (l_0), comparable with the linear dimensions of the flow domain, and the smallest dynamically significant length-scale being the Kolmogorov micro-scale, or viscous length-scale (η) (Gibbs, 2016a). Kolmogorov (1941) proposes a theory for homogenous, isotropic, incompressible turbulence, based on the similarity hypothesis that turbulence displays universal patterns, independently of initial and boundary conditions, that is, energy is added to the fluid on the inertial scale and is dissipated as heat on the viscous scales, whose motions depend only on the turbulent dissipation rate (ε) and kinematic viscosity (ν). From the previous two variables, Kolmogorov defines the dissipation length (η), time (τ) and velocity (υ) scales, described on Equations (3.1), (3.2) and (3.3), respectively. It is interesting to note that its combination results in a unitary Kolmogorov Reynolds number ($Re_{K41}=1$).

$$\eta = \left(\frac{\nu^3}{\varepsilon} \right)^{\frac{1}{4}} \tag{3.1}$$

$$\eta = \left(\frac{\nu^3}{\varepsilon} \right)^{\frac{1}{4}} \tag{3.2}$$

$$\upsilon = (\nu\varepsilon)^{\frac{1}{4}} \tag{3.3}$$

The transfer of energy is unidirectional, towards progressively smaller spatial scales across a hierarchical wave-number spectrum, being a 3D nonlinear process (Argyropoulos and Markatos, 2015). The concept of an "eddy" is useful for discussing the same mechanism, the so-called "energy cascade". An eddy can be understood as a turbulent pattern, co-existing on a volume of fluid at a wide range of wave-lengths (Tennekes et al.,1972). Considered as a tangle of vortex elements, these structures are stretched in a preferred direction by the mean flow and in any direction by one other, a process termed "vortex stretching", which ultimately leads to the breaking down of larger eddies into smaller ones. The dissipative scale is reached when the eddies lose their kinetic energy by direct action of the viscous stresses, converting it into internal thermal energy. It is important to underline that viscosity does not affect the larger-scale eddies, which are responsible for the turbulent mixing, neither plays any role on the stretching process nor does it quantify the amount of dissipated energy. Thus, the molecular kinematic viscosity (v) only determines the smallest scale at which dissipation takes place (Argyropoulos and Markatos, 2015), as described in Equation (3.1).

A second hypothesis is proposed by Kolmogorov (1941) stating that, at very high Reynolds numbers, within the inertial subrange (that is, the eddy length scale (l) respects the relation: $l_0 \gg l \gg \eta$) the kinetic energy is essentially conserved and merely transferred in that isotropic range to smaller scales, with the viscous effects being negligible. The respective mathematical formulation is recognized as Kolmogorov´s -5/3 power law, graphically illustrated in Figure 3.1. This is one of the most famous results of Kolmogorov theory, and considerable experimental evidence supports it (Frisch and Kolmogorov, 1995).

A dimensional analysis of ratio between the integral scale and Kolmogorov micro-scale shows that $(l_0 / \eta) \sim Re^{3/4}$, *i.e.* the width of the spectrum increases with the Reynolds number, or in other words, greater is the disparity between the orders of magnitude of l_0 and η. This is a primary barrier to the detailed numerical computing (as well as experimental measuring) of turbulent flows, because an enormous range of scales must be resolved, requiring computational domains with meshes so fine and, consequently, miniscule time increments that even modern computational resources are insufficient to compute an engineering solution within acceptable execution times. This observation introduces the following subchapter, where dissimilar methods to numerically model turbulence are exposed and compared.
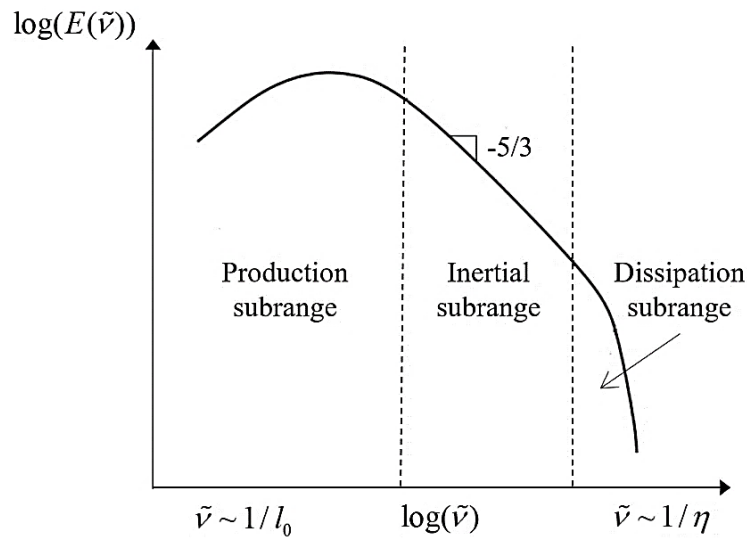
Figure 3.1. Energy spectrum as a function of the wave-number (or wave-length) (Kolmogorov, 1941).

3.2. An overview on numerical turbulence modelling methods

Turbulence modelling is the construction and employment of a mathematical model to predict the effects of turbulence. Depending on the computational resources available and the level of detail and fidelity required, the solution to turbulent flow problems can be obtained using numerical approaches of different nature, which return dissimilar levels of accuracy and costs. In some engineering applications, it may only be necessary to capture the primary features of a flow, accepting that the comprehensive turbulent solution may not be feasible to obtain, or even relevant, so reductionist flow depictions are favoured. In sum, three distinct methodologies are prevalent in CDF turbulence calculations and research, as follows.

3.2.1. Direct Numerical Simulation

Direct Numerical Simulation (DNS) is the most accurate approach to simulate turbulent flows as it involves the numerical resolution of the full three-dimensional unsteady Navier-Stokes equations without any turbulence model. The absence of a turbulence model implies that the simulation result is obtained by numerically solving all the wide-raging spatial and temporal scales of turbulence, and therefore, its precision is unrivalled by other methods (Argyropoulos and Markatos, 2015). To depict the totality of turbulent scales, the grid cell size and DNS time step should decrease proportionally to $Re^{-3/4}$ and $Re^{-1/2}$ (Reynolds, 1990), respectively. Consequently, the DNS main limitation is its overwhelming

demand on present-day computing resources (execution time and storage) when resolving high-*Re* flows. Hence, this technique is restricted to low-*Re* flows with relatively simple geometries (Zhiyin, 2015). However, DNS data is important for the development, improvement and validation of turbulence models, due to the ability to provide appropriate turbulence statistics, *e.g.* the temporal 3D distribution of scalar fields within the domain.

3.2.2. Reynolds-averaged Navier-Stokes

The Reynold-averaged Navier Stokes (RANS) approach has been the industrial CFD application backbone for the last decades, due to its relatively modest computing requirements (Zhiyin, 2015), especially when one is interested in the steady-state fluid flow solution and it is not imperative to comprehensively simulate the flow details. Hence, the fundamental purpose of the RANS method is to solve only for the averaged quantities, while the effect of all the turbulent scales and fluctuations are modelled by a particular turbulence model. For the sake of clarity, only a generic and abbreviated presentation in attempted here, restricted to a single-phase, incompressible, Newtonian fluid turbulent flow, passible to be described by the Navier-Stokes equations, overlooking external forces acting upon it.

The Reynolds decomposition, Equation (3.4), describes the turbulent motion as an arbitrary fluctuation around the mean value of a generic scalar variable (ϕ), where $\overline{\phi}$ is the time-mean value and $\phi^{'}$ the instantaneous deviation component. The scalar variable can be, for example, the local pressure or a component of the velocity vector.

$$\phi = \overline{\phi} + \phi^{'} \tag{3.4}$$

The $\overline{\phi}$ value can be computed by Equation (3.5), where Δt is a time interval much larger than the fluctuation time scale (t_1) (Markatos, 1986). Oliveira and Lopes (2016) suggest that a time interval longer than 5 seconds can, in most cases, be enough to compute $\overline{\phi}$. The Reynolds decomposition properties dictate that the time-average of the fluctuating value is zero.

$$\overline{\phi} = \lim_{t \to \infty} \frac{1}{\Delta t} \int_{t}^{t+\Delta t} \phi dt \tag{3.5}$$

Substituting Equation (3.4) into the continuity and Navier-Stokes equations, also considering constant the laminar viscosity (ν), and then time averaging the resulting expression, one derives Equations (3.6) and (3.7), where tensor notation is adopted. The latter equation is known as the RANS equation. From the Reynolds operator properties, it is simple to demonstrate that both mean $(\overline{u}_i)$ and fluctuating $(u_i^{'})$ velocity fields respect the differential mass conservation equation.

$$\frac{\partial \overline{u}_i}{\partial x_i} = 0 \tag{3.6}$$

$$\frac{\partial \overline{u}_i}{\partial t} + \frac{\partial}{\partial x_j}(\overline{u}_i \overline{u}_j) = -\frac{1}{\rho}\frac{\partial \overline{p}}{\partial x_i} + \nu \frac{\partial^2 \overline{u}_i}{\partial x_j \partial x_j} - \frac{\partial}{\partial x_j}\left(R_{ij}\right) \tag{3.7}$$

Resulting from the non-linearity of the Navier-Stokes equations, a new term appears, as shown on the right member of Equation (3.7), termed the Reynolds stress tensor (**R**). The Reynolds stress tensor is a symmetrical square matrix with six independent components, as shown in Equation (3.8). Its physical meaning in the RANS equation is the depiction of the effects of turbulent fluctuations interfering with the mean flow and its emergence results in a total of six additional unknown variables in the system, containing only four equations (Oliveira and Lopes, 2016).

$$\mathbf{R} = R_{ij} = \overline{u_i^{'} u_j^{'}} \tag{3.8}$$

The described surplus of unknow variables is termed in the literature as "closure problem" and the turbulence models are responsible for its mathematical closure, *e.g.* modelling the Reynolds stresses in terms of mean-flow quantities, as proposed by Boussinesq (1903). The Boussinesq eddy-viscosity (ν_t) approximation is based on the analogy between molecular and turbulent motions, based on the observation that, like molecules, turbulence eddies collide and exchange momentum, obeying the kinetic theory of gases (Argyropoulos and Markatos, 2015). This description is based on erroneous physical concepts, but is useful and widely used to describe turbulence (Versteeg and Malalasekera, 2007). One has to have in mind that ν_t is not a fluid property, but a flow one, and, as such, varies throughout the domain (Oliveira and Lopes, 2016). The Reynolds stresses are thus modelled by means of Equation (3.9) (Woelke, 2007).

$$R_{ij} = \frac{2}{3} k \delta_{ij} - 2 v_t S_{ij}^* \tag{3.9}$$

In Equation (3.9), k is the turbulence kinetic energy, $\mathbf{S}^*$ is the traceless mean strain rate tensor and $\mathbf{S}$ the mean strain rate tensor, defined by Equations (3.10), (3.11) and (3.12), respectively. Note that, as stated in Equation (3.6), for incompressible flows $\partial \overline{u}_i / \partial x_i = 0$, so the matrices S_{ij}^* and S_{ij} are in fact identical. The tensor symbol δ_{ij} represents the Kronecker delta.

$$k = \frac{1}{2} \overline{\mathbf{U}' \cdot \mathbf{U}'} = \frac{1}{2} \left(\overline{u'^2} + \overline{v'^2} + \overline{w'^2} \right) \tag{3.10}$$

$$S_{ij}^* = \left[S_{ij} - \frac{1}{3} \delta_{ij} \frac{\partial \overline{u}_i}{\partial x_i} \right] \tag{3.11}$$

$$S_{ij} = \frac{1}{2} \left[\frac{\partial \overline{u}_i}{\partial x_j} + \frac{\partial \overline{u}_j}{\partial x_i} \right] \tag{3.12}$$

As a side note, when evaluating the relative severity of turbulent fluctuations on a flow, the dimensionless turbulent intensity (I) is commonly employed, so it is pertinent to describe this variable, which relates to the kinetic turbulent energy my means of Equation (3.13). In the same expression, U_0 is the undisturbed flow velocity magnitude. A turbulent flow possesses low turbulent intensity when $I << 1$ (Oliveira and Lopes, 2016).

$$I = \frac{\sqrt{\frac{1}{3} \left(\overline{u'^2} + \overline{v'^2} + \overline{w'^2} \right)}}{U_0} = \frac{\sqrt{\frac{2}{3} k}}{U_0} \tag{3.13}$$

Turbulence is said to occur in isotropic conditions when $\overline{u'^2} = \overline{v'^2} = \overline{w'^2}$.

The substitution of Equation (3.9) in Equation (3.7) results in the RANS equation with the Boussinesq eddy-viscosity model – Equation (3.14) – where the pressure and velocity field variables are expressed in terms of time-averaged quantities. The isotropic part of the Reynolds stress tensor is embodied in the modified pressure term as $\overline{p}_m = \overline{p} - \rho(2k/3)$.

$$\frac{\partial \overline{u}_i}{\partial t} + \frac{\partial}{\partial x_j} (\overline{u}_i \overline{u}_j) = -\frac{1}{\rho} \frac{\partial \overline{p}_m}{\partial x_i} + \frac{\partial}{\partial x_j} \left[(v + v_t) \frac{\partial \overline{u}_i}{\partial x_j} \right] \tag{3.14}$$

To accomplish mathematical closure on the above equation system, the kinematic eddy-viscosity (v_t) is computed by a specific turbulence model. It is important to note that, being a scalar variable, turbulence models based on Boussinesq hypothesis can only reliably depict isotropic turbulence phenomena (Oliveira and Lopes, 2016). As Markatos (1986) demonstrates, dimensional analysis dictates that v_t is proportional to the product of a characteristic velocity (U_0) and length scale (L_0). In fact, the turbulence models are categorized as zero-equation, one-equation and two-equation models correspondingly to the mathematical formulation that complies with the mentioned proportionality. A comprehensive review on the eddy-viscosity computing equations, for a number of different turbulence models, can be consulted in the review paper of Argyropoulos and Markatos (2015).

3.2.3. Large Eddy Simulation

Large Eddy Simulation (LES) is originally performed in the pioneering work of Smagorinsky (1963) for simulating atmospheric flows. With the increased accessibility to ever more capable computing and storage hardware, LES has undoubtedly become one of the most promising and successful methodologies for simulating turbulent flows, reaching a level of maturity that gradually approaches it to the mainstream of engineering CFD analysis (Bouffanais, 2010; Zhiyin, 2015). Here only the explicit LES formality is presented, existing in fact other approaches under the LES umbrella such as ILES (Implicit LES), VLES (Very LES) and DES (Detached Eddy Simulation), to name a few.

This alternative modelling method does not adopt the conventional Navier Stokes time-averaging treatment (*e.g.* RANS). In LES the largest energy-containing scales are fully resolved (hence the designation "large eddy") while only the small flow-insensitive homogenous scales are modelled, designated as sub-grid scale (SGS). This results in a significantly lower computational cost when compared with DNS. Other merits of this modelling treatment are the ability to make unsteady predictions of the flow, *i.e.* display evidences about extreme events at some period of time, and the feasibility to simulate flows with very high *Re* (Gibbs, 2016b). As the large scales are resolved, responsible for most of the momentum transfer and turbulent mixing, well-detailed coherent flow structures and features are captured in LES, which makes this method much more accurate than the

equivalent RANS depiction (Zhiyin, 2015). The filtering applied in LES can be either explicit or implicit.

In the so-called *explicit* LES, the scales are separated by means of a low-pass spatial filter (LPF) applied to the Navier-Stokes equations (Lund, 2003). The LPF objective is to attenuate high frequency (*i.e.* low wave-number) turbulence features that are smaller than a prescribed characteristic cut-off scale (Δ), also called filter width, and pass low frequency (*i.e.* high wave-number) motions, leaving them unaffected. Mathematically the explicit filter is a convolution filter defined for an arbitrary scalar field variable $\phi(\vec{r},t)$ in space and time by Equation (3.15) (Sagaut, 2006).

$$\tilde{\phi}(\vec{r},t) \triangleq \phi(\vec{r},t) * G(t) = \int_{-\infty}^{\infty} \phi(\vec{r} - \vec{\xi},t) \cdot G(\vec{\xi}) d\vec{\xi} \qquad (3.15)$$

In the former expression, $\vec{r}$ is the position vector, t the time instant and G is the convolution kernel associated with the characteristic cut-off scale (Δ). Physically, a convolution is an integral that expresses the amount of overlap of one function $G(t)$, *i.e.* the filtering kernel, as it is shifted over another function $\phi(\vec{r},t)$, merging the functions with one another. Accordingly, when prescribing Δ, one has control over the required resolution and computational effort. Some common filters used in LES are the box (or "top-hat") filter, the Gaussian filter and the spectral (or sharp-cutoff) filter (Gibbs, 2016b). For a detailed and formal description of the enumerated filters, the reader may consult, *e.g.* Sagaut (2006).

In analogy with the Reynolds decomposition, one can use the filtering operation to decompose the instantaneous unknown variables (ϕ) into a resolved $(\tilde{\phi})$ and unresolved, or sub-grid (ϕ') components, as described in Equation (3.16).

$$\phi(\vec{r},t) = \tilde{\phi}(\vec{r},t) + \phi'(\vec{r},t) \qquad (3.16)$$

In sum, the LES filters respect some fundamental properties as linearity, insensitivity to constants and commutation with differentiation (temporal and spatial), but unlike Reynolds averaging operators, a twice filtered variable is not equal to a single filtered one, and the filtered sub-grid scale component is not equal to zero, unlike for the averaged fluctuating component in RANS methods. The stated properties are summarized in Table 3.1.

Table 3.1. Some LES filters fundamental properties.

Note	Properties	Formulae
Similar to Reynolds Decomposition	Constant insensitivity	$\int_{-\infty}^{\infty} G(\bar{\xi})d\bar{\xi} = 1 \rightarrow \tilde{a} = a$
	Linearity	$\widetilde{\phi + \zeta} = \tilde{\phi} + \bar{\zeta}$
	Commutation for diff.	$\dfrac{\widetilde{\partial \phi}}{dx_i} = \dfrac{d\tilde{\phi}}{dx_i}$
Dissimilar to Reynolds Decomposition	Double filtering	$\tilde{\tilde{\phi}} = G^2 * \phi \neq \tilde{\phi}$
	Sub-grid filtering	$\widetilde{\phi'} = G * (\phi - G * \phi) \neq 0$

Applying the abovementioned decomposition to the governing equations, one derives Equations (3.17) and (3.18). In Annex B is demonstrated the step-by-step derivation of the same expressions for incompressible, Newtonian fluids with constant laminar viscosity.

$$\frac{\partial \tilde{u}_i}{\partial x_i} = 0 \tag{3.17}$$

$$\frac{\partial \tilde{u}_i}{\partial t} + \frac{\partial}{\partial x_j}(\tilde{u}_i \tilde{u}_j) = -\frac{1}{\rho}\frac{\partial \tilde{p}}{\partial x_i} + \nu \frac{\partial^2 \tilde{u}_i}{\partial x_j \partial x_i} - \frac{\partial}{\partial x_j}\left(\tau_{ij}\right) \tag{3.18}$$

In the filtered momentum conservation expression, $\boldsymbol{\tau}$ denotes the sub-grid scale (SGS) stress tensor, defined by Equation (3.19), proposed by Leonard (1975) and termed Leonard decomposition. Clark et al. (1979) proposes a triple decomposition, where the SGS stress tensor results on the sum of three tensors, the "Leonard" term (L_{ij}), which expresses the interactions between the resolved scales, the "Cross" term (C_{ij}), representing the effects of SGS on large scales, and the "Reynolds" term (R_{ij}), representing the interaction amongst sub-grid scales, as formulated in Equations (3.20) to (3.22), respectively.

$$\boldsymbol{\tau} = \tau_{ij} = \widetilde{u_i u_j} - \tilde{u}_i \tilde{u}_j = L_{ij} + C_{ij} + R_{ij} \tag{3.19}$$

$$L_{ij} = \widetilde{\tilde{u}_i \tilde{u}_j} - \tilde{u}_i \tilde{u}_j \tag{3.20}$$

$$C_{ij} = \widetilde{\tilde{u}_i u'_j} + \widetilde{u'_i \tilde{u}_j} \tag{3.21}$$

$$R_{ij} = \widetilde{u'_i u'_j} \tag{3.22}$$

Contrarily to the Leonard term, which can be computed from the filtered field, the sum of the Cross and Reynolds terms must be modelled. From a modelling viewpoint, Equation (3.19) is unclosed, and the SGS stress tensor must be exclusively formulated in terms of resolved (or filtered) velocity field. The accuracy of a LES is strongly dependent of the way the SGS stresses are modelled, ensuring the adequate transfer of energy between resolved and unresolved turbulent scales (Piomelli, 1999).

The most common selection for the SGS stress tensor modelling is based on the eddy-viscosity assumption (or Boussinesq (1903) hypothesis), *i.e.* similarly to the Reynolds stresses modelling, an analogy is established between turbulent diffusion at the SGS and the physical molecular diffusion. The (traceless) SGS stress tensor is modelled by means of Equation (3.23), where ν_t^{sgs} is the kinematic sub-grid scale eddy-viscosity and $\tilde{S}_{ij}$ the filtered strain rate tensor. Note that only the deviatoric part of the stress tensor ($\tau_{ij}^{\text{d}} = \tau_{ij} - \tau_{kk}\delta_{ij}/3$) is relevant for incompressible flows, since the gradient of its trace may be absorbed into a modified pressure field ($\tilde{p}_m = \tilde{p} + \rho\tau_{kk}/3$) (Zhiyin, 2015).

$$\tau_{ij}^{\text{d}} = -2\nu_t^{\text{sgs}}\tilde{S}_{ij} \tag{3.23}$$

There are several different models of determining ν_t^{sgs}, thus granting mathematical closure. The units of ν_t^{sgs} are those of velocity times a characteristic length-scale, or kinetic energy density multiplied by a time-scale (Meneveau, 2010).

The oldest and best known model for that variable (Argyropoulos and Markatos, 2015) bears the name of Smagorinsky (1963), where the eddy-viscosity is expressed as the product of the filter width with a velocity scale (representing a Galilean invariant estimation of the velocity differences over length-scales of order Δ) also containing a dimensionless empirical parameter (Smagorinsky constant, c_s) whose value depends on the flow type (*e.g.* isotropic turbulence or near-wall bounded flow). A detailed and formulation and discussion about this model, as his alternatives, can be reviewed in Meneveau (2010). Germano et al. (1991) proposes a dynamic SGS model that couters one of the Smagorinsky model shortcomings, namely, it possesses the capacity to compute, in time and space, the abovementioned constant as the simulation progresses. The main benefit of this procedure is a improved behaviour near the walls, as the eddy-viscosity asymptotically tends to zero (Argyropoulos and Markatos, 2015).

A different approach is the *implicit* LES (ILES). When the finite volume method (FVM) is employed to numerically solve the flow governing equations, such as in CFD codes like OpenFOAM®, these are integrated over control volumes coinciding with the mesh cells. In LES with implicit filtering, no filtering operator acts on the Navier-Stokes and continuity equations, as the grid itself is regarded to be a box (or top-hat) low-pass filter (Zhiyin, 2015), and the filter width (Δ) is not directly prescribed, but rather related to the linear dimensions of the grid spacing (*e.g.* cube root of the volume of a hexagonal cell).

The main disadvantages of this method when compared with the former (explicit filtering) are, besides relatively superior truncation errors, that a truly mesh independent result can never be achieved. As the grid is refined, *i.e.* the filter width is decreased, smaller scale motions are resolved, and, in the limit, a DNS is performed. In other words, when performing implicit filtering, it is very difficult to distinct between numerical and modelling errors, hence discrediting any analysis of numerical scheme sensitivity (Zhiyin, 2015). On the other hand, as Gibbs (2016c) argues, when performing an explicit LES matching the space resolution of an equivalent implicit LES, the number of grid points required is radically superior, *i.e.* for the same execution time, there is a penalty on the solution resolution.

3.2.4. Detached Eddy Simulation

Detached Eddy Simulation (DES) is a relatively new method to numerically treat turbulence, and its suggestion by Spalart (1997) appears as a response to the computational and physical challenges associated with the reliable prediction of massively separated turbulent flows in practical geometries at real-world Reynolds numbers. When dealing with external aerodynamics studies (*e.g.* flow over aircraft and automobiles) a conflict among computational costs and solution accuracy arises when selecting between pure RANS and LES methodologies, as the small "attached" eddies populating the turbulent boundary layer formed in the vehicle surfaces possess non-affordable solution when performing a LES, and when opting for a RANS simulation, engineering accuracy in the large three-dimensional separation zones, populated with geometry-specific (non-universal) "detached" eddies cannot be achieved. The recognition of this problem drove the formulation of a hybrid RANS/LES approach.

Essentially, following the official definition of DES proposed by Travin et al. (2000), it is a three-dimensional unsteady approach, using (for both LES and RANS components) a

single turbulence model, which transitions between a sub-grid scale (SGS) model in locations where the grid density is fine enough for a LES, and a RANS model in regions where is not. The attached boundary layer (and its universal eddies) are modelled by RANS, while the large detached eddies, populating the separation regions and wakes, are fully resolved by means of a LES (of course, SGS eddies in the same locations are also modelled, but they have much less influence than the boundary layer eddies (Shur et al., 1999)). The "fine enough" grid for a LES is the one whose maximum, over all cartesian coordinates, spatial step (grid spacing in ILES) Δ, is much smaller than the turbulent flow integral length scale, l_0. As a result, likewise LES, the range of scales in a DES solution and, therefore, overall accuracy, increases as the grid spacing decreases (Shur et al., 1999).

Spalart (2009) comments that, presently, DES remains convincingly more capable than either Unsteady Reynolds-averaged Navier-Stokes (URANS) or Large Eddy Simulation (LES) when dealing with the same high-Reynolds number massively separated wake zones. As early as 1999, Shur et al. (1999) demonstrated very promising results when simulating the turbulent airflow over a NACA 0012 aerofoil at high angles of attack (compared with experimental data and RANS solutions), thus crediting the DES approach, especially when employing the Shear Stress Transport (SST) k-ω turbulence, originally proposed by Menter (1993).

4. Numerical assessment on erosion incidence

4.1. Numerical setup

For the numerical modelling, the open-source CFD finite volume code OpenFOAM® (version 6) is employed, in conjunction with the visualization and post-processing software ParaView® (version 5.6), both running on the OS Ubuntu 16.04LTS. The simulations are performed on a workstation equipped with six parallel-running Intel® *Core i*7 CPU clocked at 3.5GHz.

To solve the coupled Navier Stokes equations, the transient solver for incompressible, turbulent flows `pisoFoam` is used, which implements the PISO (<u>P</u>ressure <u>I</u>mplicit with <u>S</u>plitting of <u>O</u>perators) algorithm (Issa, 1986).

Regarding the numerical schemes, the preferred discretization scheme for the advection terms (*i.e.* divergence schemes) is second-order accurate, unbounded for the velocity and limited for scalar field advection, as first- and second-order upwind schemes (or any upwind-biased scheme in LES), although stable and robust, produce excessive numerical dissipation (Zhiyin, 2015). Both diffusive (*i.e.* Laplacian) and gradient terms are discretized using the Gaussian integration, which requires the interpolation of values from cell centres to face centres by means of central differencing, *i.e.* linear interpolation (Greenshields, 2018). As for the temporal discretization, a transient, second order implicit and unbounded scheme is adopted.

Usually, implicit schemes allow the use of relatively large time steps, but when performing a LES, the selected time step (Δt_s) must not allow the CFL (or Courant number, Co) to exceed an upper limit (Co_{max}), in order to resolve important time scales of turbulence as well other time-dependent features, while maintaining the solver stability, a condition described by Equation (4.1) in a three-dimensional case, where Δx_i is the cell size in the direction of the velocity component through the same cell, whose magnitude is $|u_i|$ (Courant et al.,1928).

$$Co = \Delta t_s \left(\sum_{i=1}^{3} \frac{|u_i|}{\Delta x_i} \right) \leq Co_{max} \tag{4.1}$$

The value of Co_{max} is typically unitary ($Co_{max}=1$) for explicit solver numerical stability. It can be larger than one for implicit solvers, when the number of corrector steps is increased and the convergence criteria is tightened. Nevertheless, if one is interested in capturing the unsteadiness of the solution, particularly when performing a LES, target CFL values must inevitably be inferior to one. During the performed simulations the maximum Courant number is kept no larger than 0.6, with the selection of a time step of $\Delta t_s=5 \times 10^{-5}$ s.

During a certain iteration, the residual is the normalized (so, independent of the scale of the problem) difference between the two members of the conservation equation being resolved when the current solution is substituted into the same expression. Therefore, it is a quantification of the numerical error of the solution. The user prescribes the solver tolerance for each unknown variable, *i.e.* a target final residual, below which the solution can be deemed sufficiently accurate (Greenshields, 2018) and the solver can eventually progress for the next time step calculation. The normalized tolerance is set at 1×10^{-6}, 1×10^{-8} and 1×10^{-9} for the kinematic pressure (p), velocity components (U_x, U_y and U_z) and turbulence scalars, *e.g.* eddy-viscosity (v_t) and kinetic turbulent energy (k), respectively. The kinematic pressure solution is substantially more expensive to compute when compared with the other variables mentioned, hence its tolerance is some orders of magnitude superior. For a detailed insight on the time and data IO (input/output) control, numerical schemes and solution control of the OpenFOAM® simulations conducted, the reader may consult Greenshields (2018).

4.1.1. Computational domain and grid

The computational domain, as well as the adopted nomenclature for each domain facet, is schematically illustrated in Figure 4.1. The boundary field is summarized in Table 4.1.
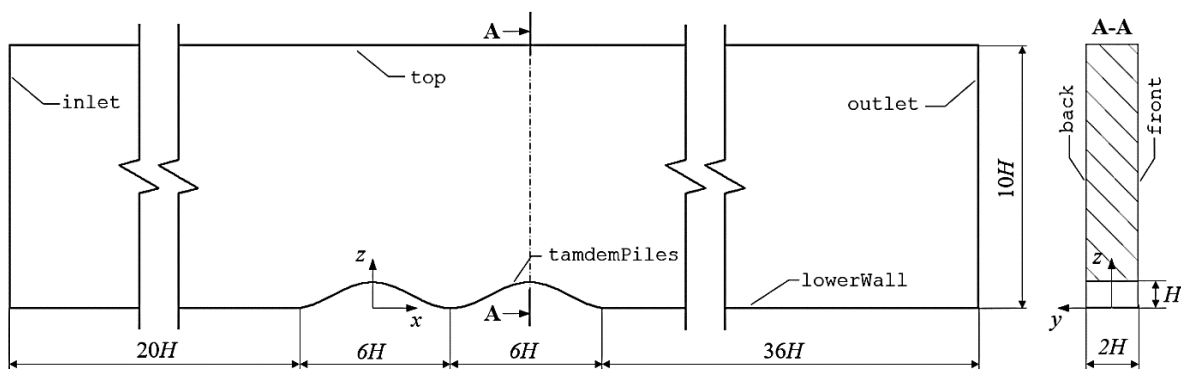

Figure 4.1. Size of the computational domain and boundary nomenclature.

Table 4.1. Boundary type of each domain face (Greenshields, 2018).

Boundary Name	Boundary Type
inlet	patch
outlet	patch
tandemPiles	wall
lowerWall	wall
top	symmetryPlane
back	symmetry
front	symmetry

For the grid discretization, the tandem piles 3D geometry is modelled in the commercial CAD software *Autodesk® Inventor* 2019 (Autodesk, 2019), and exported in stereolithographic (STL) format. The computational mesh (or grid) is generated with the OpenFOAM® supplied utility `snappyHexMesh`. This built-in utility automatically generates three-dimensional meshes, containing hexahedra and spit-hexahedra cells, from triangulated surface geometries (tri-surfaces), *e.g.* STL files. This mesh-generating tool iteratively conforms the finite volumes to the piles surfaces, refining an initial regular mesh (*e.g.* generated by the `blockMesh` utility) and morphing the resulting spilt-hex mesh to the surface, where a refinement level is specified (Greenshields, 2018). This tool also has the capability to insert cell layers in the prescribed wall-type boundaries.

The success of the grid generation process is key to the overall mesh quality (*i.e.* restricted cell non-orthogonality, aspect ratios and skewness, as well as favourable element distribution and density), and, therefore, the reliability and accuracy of the simulation results themselves. In order to perform up to the prescribed mesh quality standards, the `snappyHexMesh` utility requires high quality tri-surfaces to begin with. Thus, the rough CAD exported STL file is further treated by the OpenFOAM® surface mesh manipulation utilities `surfaceOrient` and `surfaceMeshTriangulate`. The first unifies the surface normal vectors orientation and the second imposes a refinement level that originates a highly equilateral and triangulated, closed tandem piles surface, as seen in Figure 4.2.

The computational grid is illustrated in Figure 4.3 and possesses about 1.1 million hexagonal cells. Such mesh density is from now on referred as the "medium" grid, and the following disclosure of simulation results is based on this precise spatial discretization. A formal study of the grid independence/convergence is dealt in the Section 4.2.2.
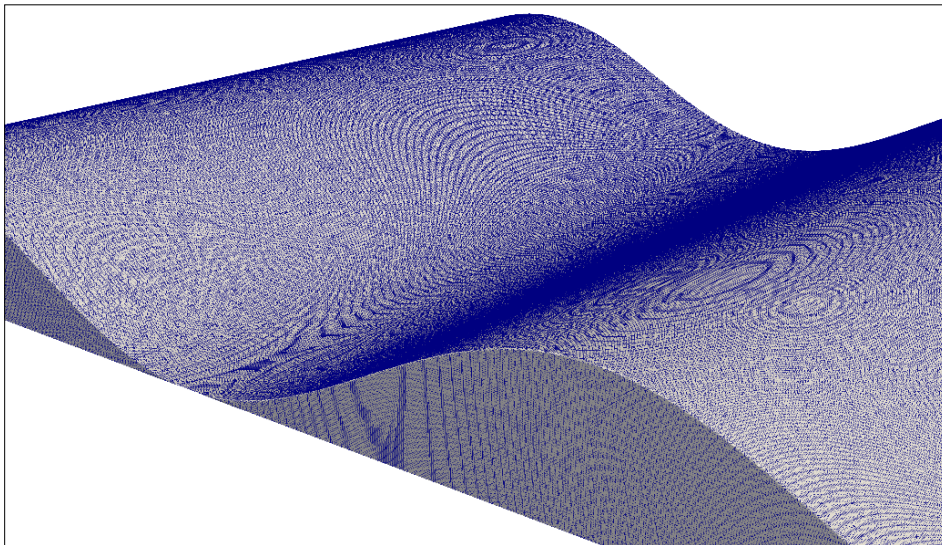
Figure 4.2. Highly triangulated, closed STL employed in the mesh generation.
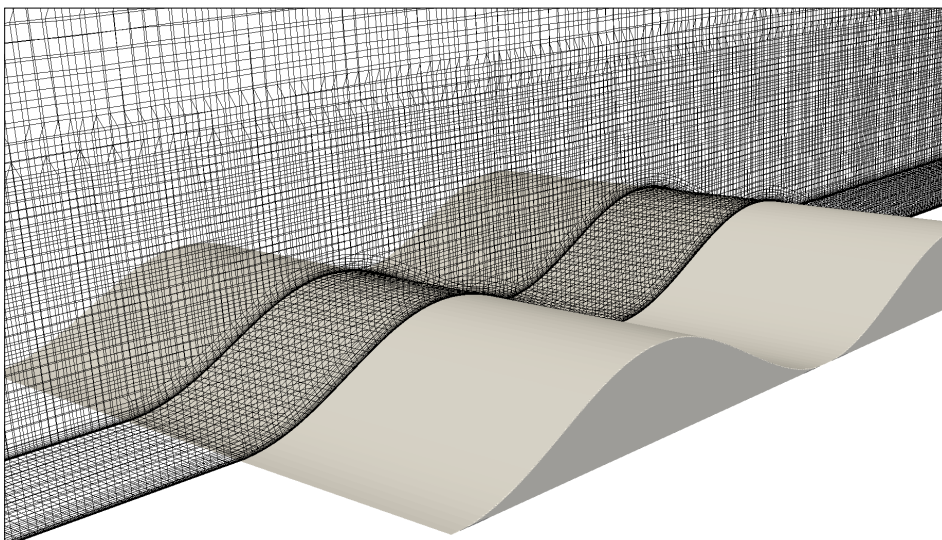
Figure 4.3. Isometric view of the `snappyHexMesh` generated grid over the tandem piles.

Since the grid generation process is discretely defining a continuous domain, the degree to which the prominent flow features are resolved, particularly when performing an ILES, heavily depends on the density and distribution of the finite volumes. For example, the prediction of separation due to an adverse pressure gradient, as the present case, hangs on the resolution of the boundary layer upstream of the separation (Ansys, 2016). Furthermore, the implicit filter width (Δ), whose value controls the lowest scale of the structures to be resolved, is set in OpenFOAM®, by default, as the cube root of the cell volume.

So, as the accurate depiction of the wall shear stress longitudinal distribution (dependent on the near-wall, surface-normal velocity gradient) is sought after, the numerical grid must allow the resolution of the viscosity-affected region, *i.e.* down to the viscous sublayer ($y^+<5$), with the first cell centre placed preferably at $y^+\leq1$ (Liu, 2016; Salim and Cheah, 2009).

To achieve the required near-wall resolution, a set of 15 cell layers is introduced on the tandem piles surface and computational domain base, with an expansion ratio of 1.3, as seen in Figure 4.4. The mean y^+ value (*i.e.* dimensionless distance from the wall to the first grid point) is evaluated at about 0.8 for the duration of the simulation.
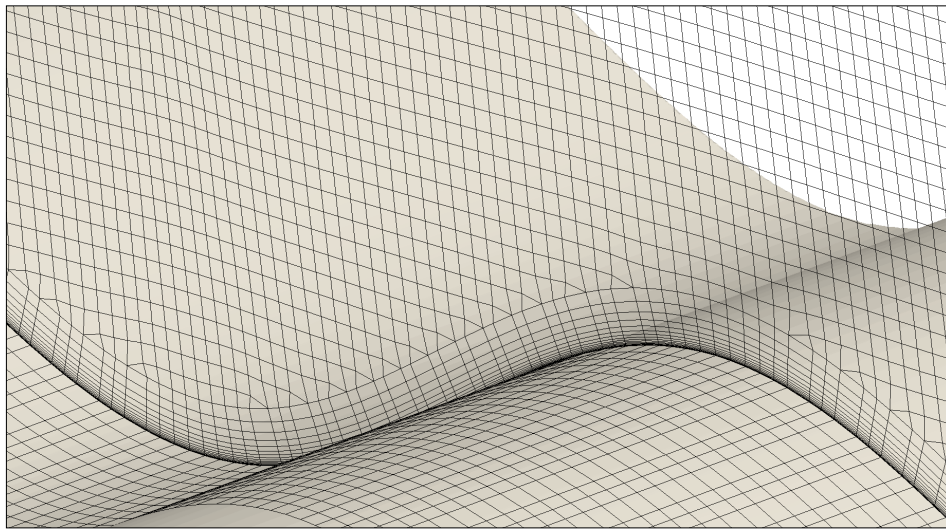
Figure 4.4. Near-wall "medium" mesh detail.

4.1.2. Employed turbulence models

Three distinct turbulence modelling approaches are compared in the numerical study: a Reynolds-averaged Simulation (RAS/RANS), a Large-eddy Simulation (LES) and a Detached-eddy Simulation (DES).

For the LES, the recently proposed sub-grid scale model `WALE` (Wall-adapting local eddy-viscosity), by Nicoud and Ducros (1999), is chosen. An advantage of the WALE model over the traditional `Smagorinsky` (Smagorinsky (1963)) model is that it returns a zero-value eddy-viscosity (v_t) within laminar shear flow regions, allowing the correct treatment of those zones in the domain. It is found that the one-equation, eddy-viscosity model `kEqn` (Yoshizawa, 1986) is uncappable to describe the wall shear stress (WSS) distribution as

experimentally probed in Ferreira et al. (2013), so it does not produce results on which a conclusion can be drawn about the prediction of wind erosion.

In regard to the RAS and DES, the built-in turbulence models `kOmegaSST` and `kOmegaSSTDES`, respectively, are tested. These models are based on the Shear Stress Transport (SST) k-ω turbulence model, first proposed by Menter (1993) and further modified in Menter and Esch (2001) and Menter et al. (2003).

The reason for the selection of this model for the present application is its proven accuracy when dealing with all-purpose bluff body aerodynamics (*e.g.* presence of adverse pressure gradients and massive separation wakes) (Menter et al., 2003) and in dune aerodynamics in particular (Liu et al., 2011).

The SST k-ω is a two-equation model, that is, besides the Navier-Stokes equations, two additional (scalar) turbulence properties transport equations are solved. In this case, one for the turbulence kinetic energy (k or TKE) and the second for the specific dissipation rate of turbulence kinetic energy (ω). The ω variable represents the rate at which TKE is converted into thermal internal energy, per unit volume and time, hence, it possesses the units of a frequency. The literature does not agree on a strict mathematical definition for the freestream value of the specific dissipation rate (ω_0). Menter (1993) initially recommends an interval of values, based on the freestream velocity (U_0) and streamwise computational domain length (L_c) – Equation (4.2). The most widely used expression implicitly uses the TKE (k) and the turbulence dissipation rate (ε) or the turbulent length scale (l), by means of Equation (4.3), where $\beta^*=0.09$ is a model constant (Lindblad 2014; Menter et al. 2003), where the subscript "0" refers to a freestream value.

$$\omega_0 = \left[1 \rightarrow 10\right] \cdot \frac{U_0}{L_c} \tag{4.2}$$

$$\omega_0 = \frac{\varepsilon_0}{\beta^* k_0} = \frac{\sqrt{k_0}}{l} \tag{4.3}$$

The boundary value for the specific dissipation rate at a solid surface (ω_{wall}) is given by Equation (4.4), where v is the kinematic molecular viscosity, $\beta_1=0.075$ is a constant and Δy_1 is the distance to the first cell-centre (Wilcox, 1988). Naturally, as the near-wall grid is further refined, and because the equation is valid only up to $\Delta y_1^+<3$, this value tends to infinity.

Reformulating Equation (3.13), the freestream TKE (k_0) expression, valid for all the turbulence models employed, reduces to Equation (4.5), where isotropic turbulence conditions are assumed. The turbulent length scale is considered to be equal to the original dune height, *i.e.* l=60 mm. Note that, at solid surfaces the no-slip condition assures that k_{wall}→0 m/s².

$$\omega_{wall} = 10 \frac{6\nu}{\beta_1 \left(\Delta y_1 \right)^2} \tag{4.4}$$

$$k_0 = \frac{3}{2} \left(I \cdot U_0 \right)^2 \tag{4.5}$$

4.1.3. Initial and boundary conditions

Concerning Figure 4.1, at the `inlet` patch, a parabolic longitudinal velocity (u) profile is implemented, governed by the described wind-tunnel measured power law – Equation (2.2). Consequently, both the turbulence kinetic energy (k) and specific dissipation rate (ω) are, likewise, functions of the wall distance (z) until z=δ, above which the freestream values U_0, k_0 and ω_0 (given by Equation (4.5) and Equation (4.3), respectively) are valid. In order to apply the defined space-varying variables, comma-separated values (.csv files) are generated and imported for each variable. On the other hand, the eddy-viscosity (`nut`) is automatically computed throughout the computational domain.

For the `outlet` patch, fully-developed conditions are assumed for the velocity and turbulent scalars. The exception is the kinematic pressure (`p`), which is set at a fixed zero-value. This is a common practice in OpenFOAM®-ran simulations, so the pressure field within the domain is relative (Greenshields, 2018).

At the solid surfaces (`tandemPiles` and `lowerWall`) , treated as wall-type patches, the no slip condition is imposed for the velocity field. The attempt to solve the boundary layer down to the viscous sublayer precludes the employment of the so-called wall functions, whose usage is aimed for grids with the centroids of the wall-adjacent cells in the log-law region, *e.g.* y^+≈30 (Salim and Cheah, 2009). Instead of resolving the full boundary layer, the wall functions model the viscous effects. Consequently, roughness is not accounted for, as its characterization implies the use of that type of boundary conditions. However, in Faria et al. (2011) and Ferreira et al. (2013) a computational parametric study on the sand grain roughness parameter (K_s, as a fraction of the particle main diameter) demonstrates only a

slight sensitivity on the same parameter, regarding the C_f longitudinal distribution on a single triangular and sinusoidal pile, correspondingly.

On the remaining domain boundaries (`front`, `back` and `top`) the simplifying `symmetry` boundary conditions are employed, reducing the overall computational execution time. The employing of these non-specific conditions at the lateral domain patches, suggest a three-dimensional nature to the problem, this being a key characteristic of turbulence.

Due to space constrains the boundary conditions and respective initial values for each of the unknown variables are not tabled in this section. For a comprehensive review, the reader may consult Appendix A, where the respective, commented dictionaries are attached and the used equations labelled.

4.2. Numerical solutions and discussion

In this subchapter the numerical predictions on the skin friction coefficient (or friction velocity) distribution are disclosed and confronted with the wind-tunnel measurements of Ferreira et al. (2013). One must emphasize that the present comparison is only valid for the original un-eroded configuration, as the overtime reshaping into intermediate profiles would definitively alter the C_f distribution, rendering unfeasible the correlation between numerical and experimental results (attained only for an undeformable sinusoidal outline).

The total simulated time is four seconds, from which only the last two are made use of (*e.g.* for averaging purposes), hence, within this short time interval, dune reshaping is not accounted for. This hypothesis is compatible with the wind-tunnel observation of Ferreira and Fino (2012), where, as seen in Figure 2.4, noteworthy profile evolutions, although being a continuous process, occur on a greater time scale.

4.2.1. SST k-ω DES model results

The simulated, time-averaged, skin friction coefficient longitudinal distribution is plotted in Figure 4.5 against the corresponding probed values in Ferreira et al. (2013). Bearing in mind the adopted coordinate system, depicted in Figure 4.1, the simulated values are evaluated at a vertical plane that splits the domain in half (*i.e. y*=0), along a set of evenly spaced (10 mm apart), virtual, wall shear stress (WSS) probes. In the same illustration, the prior formulated wind erosion threshold curves are also plotted, both the conventional Howard (1977) and the newly proposed "apparent" thresholds, for *A*=0.18.

As Ferreira et al. (2018) argues, the *A* constant is set equal to 0.18 since it is the minimum value bellow which erosion is predicted at the windward pile, therefore, the constant is established in order to conform with experimental observations and lies well inbounds of the [0.1, 0.2] interval proposed by Shao and Lu (2000).

Regarding the WSS distribution, despite some divergences at the downwind dune, it can be concluded that the computational prediction generally agrees with the experimental results. One might argue that the simulated mean C_f is overestimated at the second dune (particularly at the corresponding stoss slope), but the measuring probes in Ferreira et al. (2013) are Irwin-type pressure probes, whose accuracy is somewhat questionable, as they compute the WSS from a pressure difference, based on a calibration performed in Faria et al. (2017). An analogous comment can be held concerning the corresponding mean friction velocity distributions of the RAS and LES approaches, disclosed in the next sections.
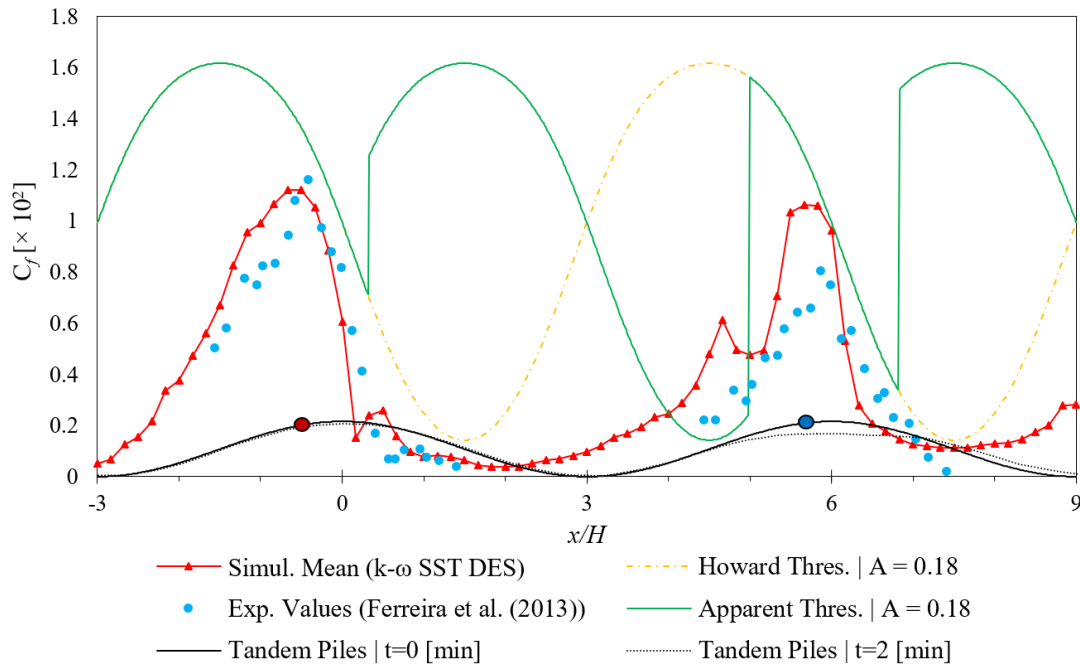
Figure 4.5. Time-averaged skin friction coefficient distribution on a convergent grid, $t \in [2,4]$ s.

Nevertheless, regarding Figure 4.5, it is important to appreciate some dune dynamics key features, as found experimentally and numerically in the work of Wiggs et al. (1996) and Ferreira et al. (2013), to name a few. Firstly, the acceleration of the attached flow along the windward side of the first dune creates a shear stress gradient along the same slope. Secondly, and a consequence of the former, it is interesting to note that the maximum (time-averaged) C_f values occur just upstream of the crest, as evaluated by the Irwin probes.

Then, within the interdune region and at the vast portion of the leeward side of both piles, as commonly found in recirculation zones, the friction velocity is relatively modest and aeolian erosion activity is reduced. This behaviour and flow topography are not exclusive to the dealt DES, as the RAS and LES exhibit similar patterns, with the turbulence models SST k-ω (Menter et al., 2003) and WALE (Nicoud and Ducros, 1999), respectively.

Regarding the numerical prediction on aeolian erosion occurrence, for each dune of the tandem arrangement, an interpretation can be drawn. At the upwind pile, the "apparent" friction velocity threshold (u_{*at}), and even the Howard (1977) threshold, is never surpassed by the mean u_*, an indication that no erosion is expected to occur at that dune, which complies with the experimental observations of Ferreira and Fino (2012), for U_0=8.3 m/s. Contrarily, at the downwind pile, there is a region in the stoss slope (roughly $x/H \in [4,5]$) where, in average, the u_* distribution exceeds the local u_{*at}, *i.e.* wind erosion is susceptible to befall at that structure.

In Figure 4.5 both the original and eroded (after 2 minutes) outlines are plotted. One is entitled to argue that, as the wind eroded region (roughly $x/H \in [5,9]$) does not overlay the $x/H \in [4,5]$ interval, where the simulation forecasts a surplus of the time-averaged u_* in relation to u_{*at}, the numerical prediction of aeolian erosion at the downwind pile is misplaced and erroneous. If the erosion mechanism was exclusively the *creeping*, this comment would be appropriate. However, given the particle diameter of the sand grains, as already mentioned in Section 2.1, it is the *saltation* erosion-process that predominates over the other mechanisms. That said, it is believed that the particles are elevated from the erosion-prone stoss slope by the aerodynamic, driving forces, near the $x/H \in [4,5]$ region, following (momentarily) the interdune flow current lines and then returning to the sand bed, downstream of the starting point, where they collide with resting grains, ejecting them in greater numbers, in a cascade-like phenomenon that ultimately leads to a larger erosion intensity in the vicinity of the crest, as observed in Figure 2.4. In Figure 4.6 is illustrated, by means of a LIC (Line Integral Convolution) surface (Loring et al. (2014)), an evidence of the simulated interdune recirculation zone attained with the SST k-ω DES model.
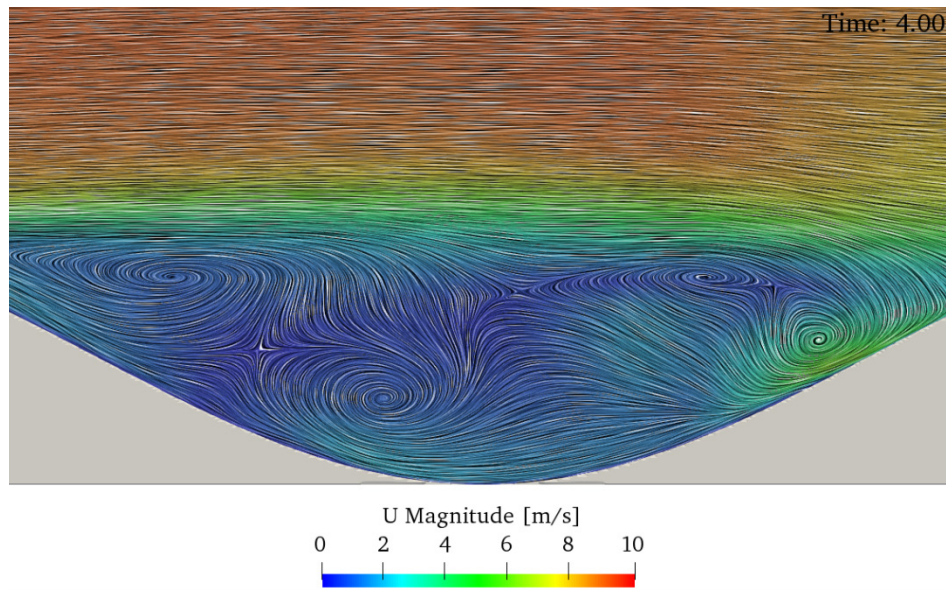
Figure 4.6. Surface LIC of the interdune simulated flow topography, at t=4 s (Loring et al., 2014).

Once established that saltation is the active erosion process, one must take into account the manifestation of burst phenomena, or burst activity (Carneiro et al., 2015), *i.e.* besides the reductionist study of time-averaged results, it is pertinent to evaluate the instantaneous friction velocity at some other locations, inferring the presence or absence of regions where the friction velocity exceeds only momentarily the corresponding local threshold.

For the effect, the time-evolving friction velocities (u_*) at the highlighted points in Figure 4.5 (x/H=-0.5 and x/H=5.67) are compared with their respective local thresholds (u_{*t} and u_{*at} overlap in those locations), in Figure 4.7. The selection of this pair of points is somewhat arbitrary, and it is simply based on the observation that the maximum time-averaged u_* occurs near those locations for each pile, that is, x/H=-0.5 and x/H=5.67, for the upwind and downwind dunes, respectively.

The Figure 4.7 graph is a strong evidence of the highly transient burst phenomenon. In the selected point of the downwind pile (x/H=5.67) unsteadiness is clearly present, as the friction velocity oscillates vigorously, often exceeding the corresponding threshold, *i.e.* although the mean u_* at that site is inferior to the local threshold (see Figure 4.5), erosion will, at some brief instances, take place. In opposition, the instantaneous u_* at the windward point (x/H=-0.5) unreliably evidences a nearly steady value, always lower than the respective threshold. Without going into detail, such prediction is due to the DES turbulence model properties and, with some insight to the WALE-LES simulation, it is not an accurate depiction of the transient, chaotic nature of turbulence and wind-driven erosion processes.
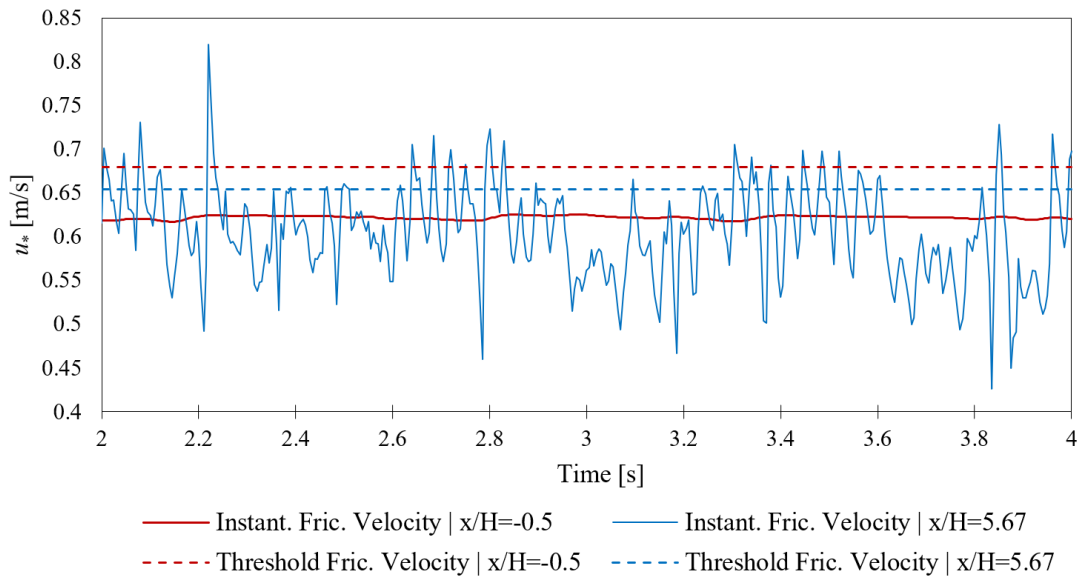
Figure 4.7. Instantaneous friction velocity and respective thresholds at x/H=-0.5 and x/H=5.67.

For a comprehensive analysis on the aeolian erosion-prone locations, in Figure 4.8 is assessed the minima and maxima of C_f along the full extent of the tandem arrangement, without concerning the time instant of its occurrence. Note that, at the windward pile, there is an almost superposition of the minimum and maximum friction velocities, up until just downstream of its crest (including the former examined x/H=-0.5 point), seemingly indicating the non-existence of instantaneous fluctuations of u_* within that region.
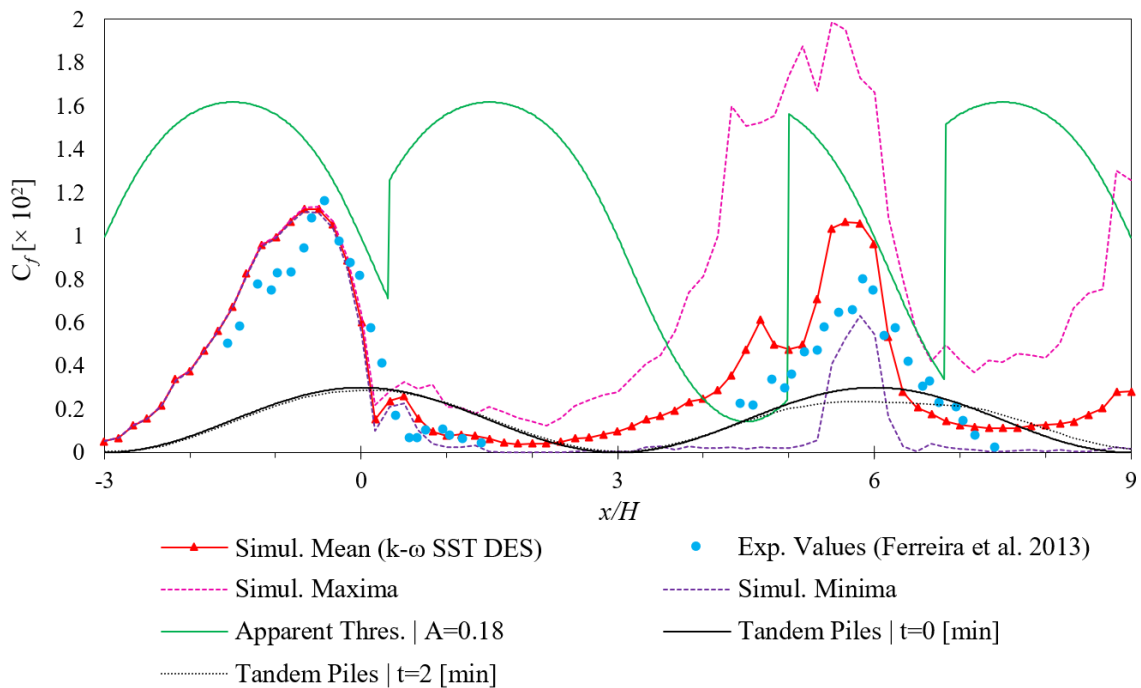
Figure 4.8. Distribution of the skin friction coefficient minima and maxima (SST k-ω DES prediction).

This non-coherent behaviour is due to the RANS approach being active in that attached (boundary layer) flow region, consequently converging to a nearly steady-state solution, which although perfectly capable of evaluating the time-averaged WSS distribution, is uncapable to portray transient phenomena. Leeward from the separation point ($x/H \approx 0.33$) the DES transitions to a LES, as the grid is sufficiently fine and a massive recirculation zone is found, leading to the portrayal of an increasingly larger amplitude between the local maximum and minimum u_* as one progresses further downstream. Again, this is an evidence that unsteadiness is, from that point on, being numerically predicted, thus the ability to depict phenomena like burst activity.

From Figure 4.8 is clear that the SST k-ω DES simulation predicts wind erosion not only on an average basis (roughly at $x/H \in [4, 5]$), but also transitorily, along a broader span of the leeward dune (roughly at $x/H \in [3.5, 6.5]$). This remark further supports the observation of a greater erosion activity near the crest, also due to the abovementioned, speculated saltation particle transport effects.

On a side note, the position of the separation and reattachment points, *i.e.* the time-averaged coordinates of the $(x/H)_R^i$ points of Equation (2.6), whose values control the "apparent" threshold curve, are evaluated in this precise simulation, and equally adopted for the following turbulence models results, as the SST k-ω DES possesses, bearing in mind the literature review on the subject, the best faculties to properly reproduce those regions (Spalart, 2009). The corresponding longitudinal, mean coordinates are listed in Table 4.2.

Table 4.2. Time-averaged locations of the start (i=1) and end (i=2) points of the recirculation zones.

Interdune region		Lee slope of windward pile	
$\left(x/H\right)_R^1$	0.33	$\left(x/H\right)_R^1$	6.83
$\left(x/H\right)_R^2$	5.00	$\left(x/H\right)_R^2$	9

4.2.2. Quantification and bounding of numerical uncertainty

One of the challenges encountered when performing CFD simulations is determining the level of accuracy of the numerical predictions. Typically, this is accomplished by comparison of the computational results with the available experimental data, but this tactic does not contemplate the inherent errors and uncertainties which are undoubtedly present in the numerical calculations (Karimi et al., 2012).

To quantify this numerical uncertainty Roache (1994) proposes a practical, systematic method for the uniform reporting of grid-convergence studies and numerical error bounding, using the so-called Grid Convergence Index (GCI), which is based on the generalized Richardson (1911) extrapolation and involves the comparison of discrete solutions at two different grid spacings.

Before advancing, one must recognize the difference between a numerical result which approaches its asymptotic numerical value and one which approaches the true solution. It is expected that, as the grid is further refined and the resolution improved, the computed solution will not significantly alter, approaching an asymptotic value (*i.e.* the true numerical solution) (NPARC, 2008). Most certainly there will still be errors between this asymptotic value and the true physical solution to the equations, due to other error sources, namely the input uncertainty and model uncertainty (Freitas, 2002). To minimize the first, all the input constants and parameters are specified with a high level of accuracy (to five significant digits), and the former is restricted by the proper choice of the solver and a turbulence model study.

Therefore, the GCI is a measure of the percentage of how much the computed value is away from the numerical asymptotic value, in the form of an error band, *i.e.* it indicates how relevant is the further refinement of the grid. A small value of GCI indicates that the result lies within the asymptotic range (NPARC, 2008). However, remember that a truly mesh independent result can never be achieved when performing an implicit LES, as explained in Section 3.2.3. This study is exclusively executed with the *SST k-ω* DES model results.

In order to apply the GCI, three simulations with three different grids of spacing h_1, h_2 and h_3 are required, respectively representing the fine, medium and coarse mesh resolutions. Richardson (1911) extrapolation dictates the formula for a higher-order estimation of the continuum value (value at zero grid spacing, $f_{h=0}$) from a series of lower-order discrete values. If one assumes a second-order numeric solution and has computed the simulated quantity (f) on two grids, one finer (f_1) and the other coarser (f_2), the value for $f_{h=0}$ can be estimated by means of Equation (4.6), where $r=h_2/h_1$ is the adopted grid refinement ratio.

One use of the calculated continuum value ($f_{h=0}$) is to report an improved, third order accurate, estimate of the CFD-computed f_1. The other use of $f_{h=0}$ is to obtain an evaluation of the discretization error associated with the fine grid (NPARC, 2008).

$$f_{h=0} \cong f_1 + \frac{f_1 - f_2}{r^2 - 1} \tag{4.6}$$

The GCI method by Roache (1994) is based on the outlined above, the first step being the estimation of the fractional Richardson error in the fine grid solution (E_1), also designated normalized discretization error – Equation (4.7). In that expression, p is the formal order of accuracy (or order of convergence rate), which can be computed by Equation (4.8), where f_1, f_2 and f_3 are the numeric solutions for the fine, medium and coarse grid resolutions, respectively. The symbol ε_1 represents the relative error, calculated by Equation (4.9).

$$E_1 = \frac{|\varepsilon_1|}{r^p - 1} \tag{4.7}$$

$$p = \ln\left(\frac{f_3 - f_2}{f_2 - f_1}\right) / \ln(r) \tag{4.8}$$

$$\varepsilon_1 = \frac{f_2 - f_1}{f_1} \tag{4.9}$$

The GCI for the fine grid (GCI$_{fine}$ or GCI$_{1-2}$) is expressed in Equation (4.10), where F_s is an empirically determined safety factor that converts the normalized error (E_1) into a 95% confidence interval, uncertainty estimate (Roache, 1994). For comparations over three or more grids, F_s=1.25 is advised. It is important that each grid level yield solutions that are within the asymptotic range of convergence (NPARC, 2008). This can be observed by Equation (4.11).

$$\text{GCI}_{fine} = F_s \cdot E_1 \times 100 \tag{4.10}$$

$$\text{GCI}_{2-3} = r^p \cdot \text{GCI}_{1-2} \tag{4.11}$$

The three mesh schemes tested are characterized in Table 4.3. Some relevant features are the grid spacing at zero level (δ_0, equal in all cartesian directions), the number of cells in the transverse direction (N_y), the total number of cells (N_{total}) and the respective execution times (Δt_{exec}). The fine and coarse grid features are similar to those exposed in Section 4.1.1.

The adopted grid refinement ratio (GRR) is r=1.2, which is greater than the minimum of r=1.1 proposed by Roache (1994), as the employment of lower values hamper the differentiation between discretization errors from other sources, such as iterative

convergence errors and computer round-off (NPARC, 2008). When $r=1.33$ is adopted, a fully RANS simulation is executed on the coarser grid, not a DES. Moreover, the near-wall resolution should, in any case, permit a $y^+ \leq 1$, hence the restrictive selection of a lower value for r. Note that, even with this modest GRR, the execution time increases drastically as one goes up on the refinement hierarchy, so limitations in computing resources are also present.

Table 4.3. Mesh properties for the GCI study ($r=1.2$).

Mesh	δ_0 [mm]	N_y [cells]	N_{total} [cells]	Δt_{exec} [h]
Coarse	24	20	8.39×10^5	88.5
Medium	20	24	1.14×10^6	219.8
Fine	16.67	28	1.80×10^6	368.2

In Figure 4.9 the mean C_f distributions on the prescribed grids are confronted along the tandem pile arrangement. From the graphic consultation, one can positively claim that there is a satisfying agreement between the results for the dissimilar grid densities throughout the domain.
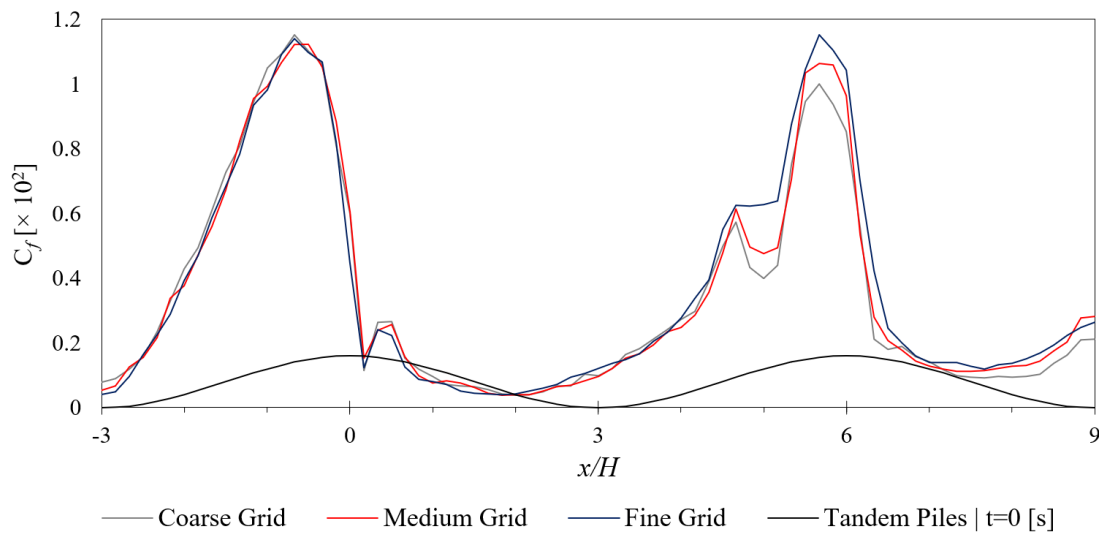
Figure 4.9. Comparison between the mean skin friction coefficient distribution of the three grids ($r=1.2$).

For reasonable evaluation of the GCI results, it is key to anticipatedly point out the implications of the employment of such low grid refinement ratio ($r=1.2$) on the normalized discretization error (E_1) and GCI. In regard to Equation (4.7), it is important to have in mind that the denominator tends to decrease in value, as the GRR is reduced (for any prescribed order of convergence rate, p). There comes a point that the denominator descends to values inferior to one, thus leading to enhanced GCI values, even with small associated relative

errors (ε_1). For the effect, Roache (1994) presents a guideline for GCI$_{fine}$ values for common r and p combinations, listed in Table 4.4, for a normalized relative error of ε_1=1 %.

Table 4.4. GCI values for typical combinations of r and p, ε_1=1 % (Roache, 1994).

		Fine grid GCI	
p	$r = 2$	$r = 1.5$	$r = 1.1$
1	3.00 %	6.00 %	30.00 %
2	1.00 %	2.40 %	14.29 %
3	0.43 %	1.26 %	9.06 %

In Figure 4.10 is shown a graph of the time-averaged friction velocity as a function of the grid resolution, namely the total number of nodes in the grid, at evenly spaced locations. The selected quantity of interest, as well as the points of evaluation, are chosen arbitrarily.
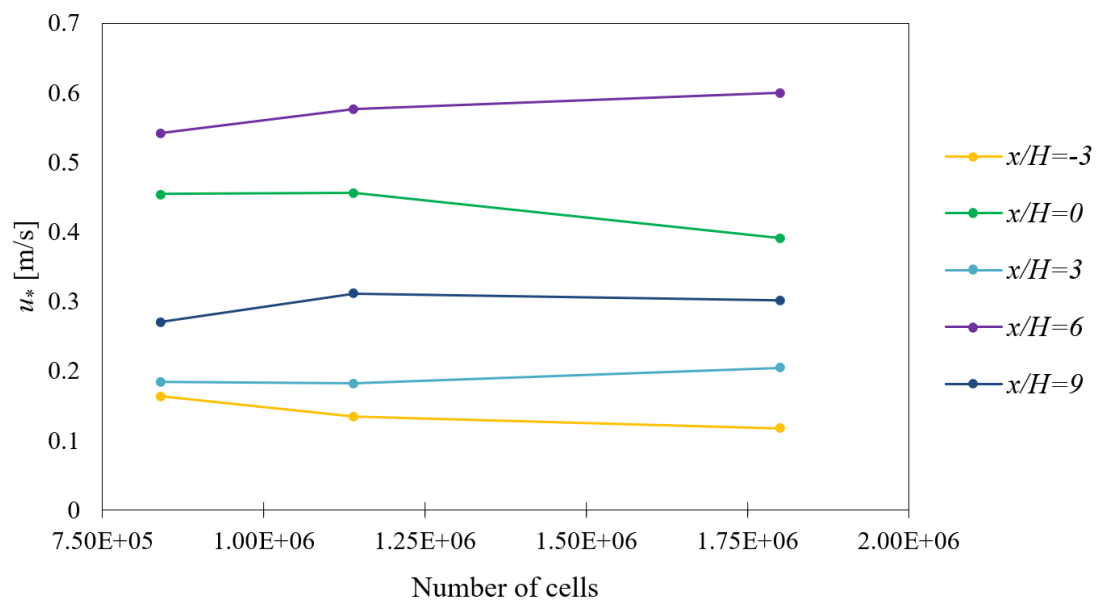
Figure 4.10. Grid sensitivity curve for the mean friction velocity at some regular coordinates.

As Freitas (2002) argues, grid sensitivity curves like the one illustrated in Figure 4.10 are characterized by a monotonic region of rapid convergence, followed by a non-monotonic, asymptotic region of slow convergence. The order of convergence rate must be computed in that asymptotic area, by means of Equation (4.8).

In Table 4.5 are evaluated the local order of convergence rate (p_{local}), the respective relative errors (ε_1 and E_1) and GCI$_{fine}$ at the given points. Note that the logarithmic properties dictate that the p_{local} can only be computed from monotonic curves, _e.g._ x/H=-3 and x/H=6.

Freitas (2002) suggests that it is prudent to discretely calculate p at locations of interest, however, to globally describe the simulation numerical error, a single, averaged value is preferable. The same is true for stating the uncertainty or error of a given parameter.

Table 4.5. Summary of grid sensitivity analysis.

x/H	p_{local}	$\lvert\varepsilon_1\rvert$ [%]	E_1 [%]	GCI_{fine} [%]
-3	2.65	14.87	33.02	41.27
-1.5	-	0.91	2.01	2.51
0	-	16.60	36.88	46.10
1.5	-19.89 (N.A)	18.89	41.95	52.44
3	-	11.07	24.58	30.72
4.5	-	6.72	14.93	18.65
6	2.14	3.85	8.56	10.69
7.5	1.33	6.39	14.20	17.76
9	-	3.31	7.35	9.19
Average	2.04	9.18	20.39	25.48

The local values of p (when applicable), as well as the corresponding mean value, are consistent with the global, theoretical order of accuracy of the code, which is second order accurate (p=2), therefore, the overall simulation results lie in the asymptotic range. The negative value at x/H=1.5 indicates that the solution of the fine grid diverges from the medium grid result at that wind erosion resistant location, *i.e.* the solution is not in the asymptotic region at that point. Inclusively, in the same site, the GCI is the largest from the studied sample. Generally, the points corresponding with the erosion-prone downwind pile ($x/H \in [3, 9]$) exhibit lower GCI percentage (around 17.40 %, in average).

To close this section, one must underline that Roache (1994) GCI uncertainty-reporting method is quite conservative (NPARC, 2008). The bounded, time-averaged friction velocity at any point of the solution domain, or at any point of the leeward dune surface, can be calculated by Equation (4.12) and Equation (4.13), correspondingly. If the workstation computing resources were more advanced, the study of a higher level of refinement would be appropriate and the consequent numerical error evaluation better suited.

$$u_*^{bounded}(x,y,z) = u_*(x,y,z) \pm 0.2548 \cdot u_*(x,y,z) \tag{4.12}$$

$$u_*^{bounded}(x,y,z) = u_*(x,y,z) \pm 0.1740 \cdot u_*(x,y,z) \tag{4.13}$$

4.2.3. SST k-ω model results

Employing the SST *k-ω* RANS (Menter et al., 2003) turbulence model, the solution converges to a nearly steady-state solution, in which the time-averaged skin friction coefficient distribution is almost indistinguishable, for a good part of the tandem pile extent, from the respective minima and maxima curves, as seen in Figure 4.11.

This behaviour, already observed in the SST *k-ω* DES model at some attached-flow locations, is an indication that a RANS simulation is, by itself, insufficient to predict aeolian erosion manifestation along these structures, as it fails to depict the unsteadiness of the problem, *i.e.* the existence of wide-ranging fluctuations in the u_* distribution (burst phenomena).

Note that the RANS simulation is labelled as an insufficient approach, and not an uncappable one. In fact, with the adoption of a proper model for the threshold curve (u_{*at}), as depicted in Figure 4.11, wind erosion is still predicted at the stoss slope of the second dune by the accurate computation of the WSS, and no erosion is expected to arise at the first, as observed experimentally. The main shortcoming is due to the reductionist prediction of the erosion affected area, but the RANS solution benefits from an inferior execution time, when compared with the DES and LES counterparts.
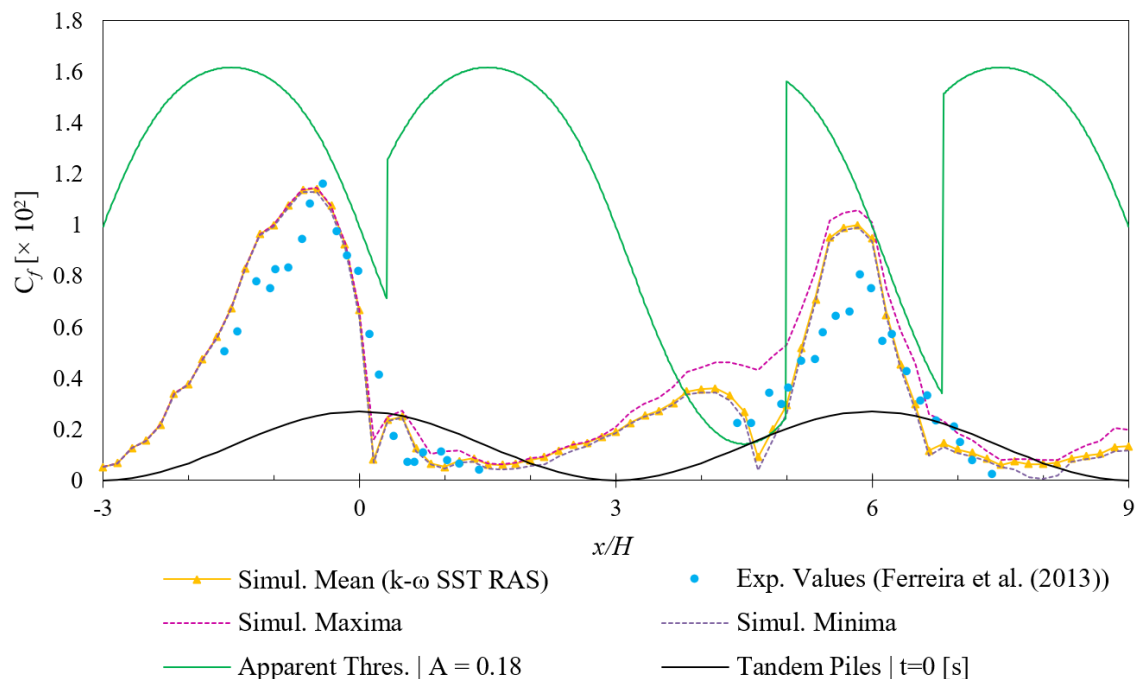
Figure 4.11. Distribution of the skin friction coefficient minima and maxima (SST *k-ω* prediction).

4.2.4. WALE model results

In disparity with the previous models, the WALE SGS turbulence model (Nicoud and Ducros, 1999), entirely accounts unsteadiness throughout the computational domain. Indeed, as illustrated by the C_f distributions of Figure 4.12, at any longitudinal coordinate there is a considerable discrepancy amongst the mean, minimum and maximum values, evidencing that the local friction velocity oscillates with a sizable amplitude.

Note that even at the windward dune, although perfectly invulnerable to wind erosion on a time-averaged basis, the maxima curve surpasses the "apparent" threshold curve in some zones (specifically, in the neighbourhood of its crest), meaning that brief bursts of particle migration would momentarily occur from that pile. This observation is exclusive to the LES approach, as neither the former turbulence treating methods could explain the very limited, but existent, aeolian reshaping in the upwind pile, as observed in Figure 2.4.

Additionally, the WALE-LES model predicts an absolute maximum about 20% greater than the forecast by the SST k-ω DES model, as well as other peak values, in locations different from the one where the average maximum value occurs, and the overall erosion-prone area at the downwind pile is slightly wider when compared with the DES prediction. Moreover, this model possesses a unique behaviour for the time-averaged C_f, as the respective curve is virtually identical for the windward and leeward dunes, demonstrating an almost insensitivity to the interdune interference in that regard.
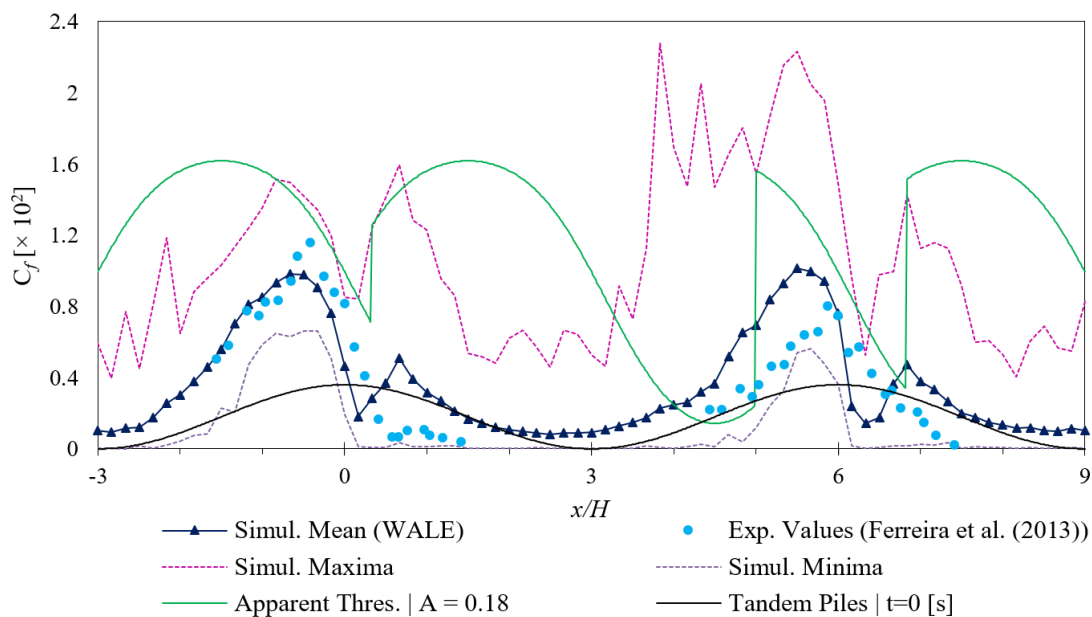
Figure 4.12. Distribution of the skin friction coefficient minima and maxima (WALE prediction).

In Figure 4.13 the mean C_f distributions, for each turbulence treating approach, are confronted and some interesting observations arise. In general, the curves follow a trend, with the major discrepancies occurring in the vicinity of the threshold curve discontinuities, *i.e.* near the separation or re-attachment points. In those regions, it is the computational resources-sparing RANS approach that better agrees with the wind-tunnel probed values. Note how, up until the first separation point, the SST k-ω and SST k-ω DES model curves are undistinguishable, an evidence that the DES is performing a RAS upwind from that point.

Another remark is that, contrarily to the RAS and DES, the LES predicts a monotonic increase of the friction velocity at both the windward and leeward dune stoss slopes, in agreement with the experimental evolution in those regions. However, this LES model seems the least conforming to the WSS experimental measurements, *e.g.* it even forecasts a greater mean C_f at the downwind pile. Despite this, the WALE model results turn out to be the best fitting to explain the tandem pile aeolian reshaping as observed experimentally in Ferreira and Fino (2012).
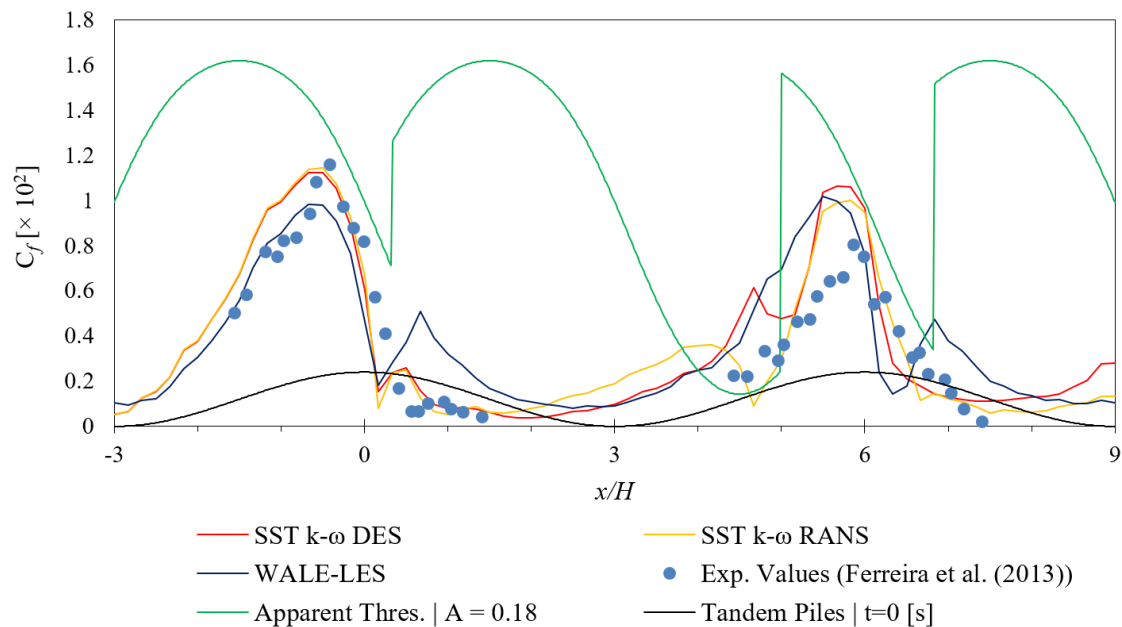
Figure 4.13. Distribution of the mean skin friction coefficient for different turbulence models, $t \in [2,4]$ s.

5. Conclusions

The present work reports a CFD study on the numerical prediction of the wall shear stress distribution along a set of closely spaced, sinusoidal, tandem sand piles, orthogonally placed in relation to the incoming wind flow, relating it with the observed aeolian erosion. For this purpose, in an introductory manner, in Chapter 2 some foremost comments are drawn in regard to the theory of aeolian erosion and the experimental, wind-tunnel reshaping observations for the same arrangement and conditions. The key observations in Chapter 2 are described below.

i. The wind-tunnel, time evolving, profile measurements conducted in Ferreira and Fino (2012), for the prescribed geometry and undisturbed wind velocity, reveal that the upstream pile remains practically unchanged, while the downstream pile is considerably eroded over time.

ii. The wall shear stress distribution (τ_w), or the corresponding, literature-favoured, friction velocity (u_*), is of primary importance when describing wind erosion phenomena, as the onset of aeolian particle migration from a surface occurs whenever the u_* locally exceeds the so-called friction velocity threshold (u_{*t}).

iii. The concept of burst activity is introduced, which is a highly transient phenomenon, associated to the saltation erosion mechanism. It can be understood as intermittency on the erosion process, as the values of u_* dynamically fluctuate.

iv. Under idealized conditions, the friction velocity threshold can be modelled as a function of the predominant grain diameter. Some classic formulations of u_{*t} are those of Bagnold (1941) and Howard (1977), valid for particles resting on horizontal and arbitrarily oriented aeolian surfaces, respectively.

v. In order to comply with the development of the experimentally observed, sizable recirculation zones at the interdune and lee slope of the downwind dune regions, a reformulation of the customary Howard (1977) curve is proposed and adopted, termed in this document "apparent" threshold friction velocity (u_{*at}).

Regarding the CFD simulation results, presented in Chapter 4, three different turbulence modelling methods are compared, *i.e.* the Reynolds-averaged Navier-Stokes (RANS), the Large Eddy Simulation (LES) and the Detached Eddy Simulation (DES), with the adoption of the turbulence models SST k-ω, SST k-*ω* DES and WALE (Nicoud and Ducros, 1999), respectively. The foremost conclusions drawn from the results are listed below.

i. In general, for the three models, the corresponding time-averaged, longitudinal skin friction coefficient distributions agree with the experimental measurements carried out in Ferreira et al. (2013), with an overestimate at the downwind crest.

ii. As observed in the wind-tunnel experiments, large recirculation bubbles are computationally predicted, particularly at the interdune region.

iii. In a time-averaged basis, all the three methods predict the occurrence of aeolian erosion at the stoss slope of the downwind pile, as well as the absence of the same phenomenon at any location of the upwind pile. This is a key observation, compatible with the reshaping observations of Ferreira and Fino (2012).

iv. A formal grid refinement study, employing the Grid Convergence Index (GCI) proposed by Roache (1994), conservatively bounds the numerical uncertainty of the friction velocity solution. Overall, the results appear to be in the asymptotic region, but a further refinement would be appropriate to reduce the GCI percentage, which is impracticable with the available computational resources.

v. By itself, a RANS approach is insufficient to reliably describe the erosion process, as it fails to depict the unsteady nature of the problem, with its friction velocity solution converging to a nearly steady-state value throughout the tandem piles extent. However, the RANS approach is perfectly capable (and even more accurate in that regard than the other studied methods) to describe the longitudinal wall shear stress distribution.

vi. Conversely, a LES (or DES, in some regions) approach is capable to depict the highly transient burst activity phenomenon, as the friction velocity solution dynamically fluctuates, with a sizable amplitude, around a mean value. Thus, the LES method entirely describes the wind erosion manifestation, not only on a time-averaged basis, but also in a localized, instantaneous manner, which ultimately leads to the prediction of a wider erosion-prone area.

Suggestion for future work

A topic that is not covered in this document is the benchmarking of different inlet conditions, a procedure particularly important when performing LES (Zhiyin, 2015). The bibliography is extensive in regard to the theme, and some dissimilar methods have been developed in the past years, which seek to generate a wide range of flow fluctuations around a mean value, with specified spectral properties, as intensity and length scales. Note that, for the simulations reported in this work, are imposed, solely, fixed profiles (for velocity and velocity-dependent turbulent properties) as inflow boundary conditions, so no turbulence structures are present at the inlet of the domain.

Some first steps were taken on this challenging problem, with the expensive simulation of the so-called "recycling method", also called internal plane mapping, where the computational domain is extended and the flow quantities of interest extracted from a cross-section at a certain, distant downstream point, and remapped onto the inlet (Montorfano et al., 2013).

Also, regarding the so-called "precursor method", where the inflow turbulent fluctuations are produced by an auxiliary simulation (Zhiyin, 2015), which voluntarily generates turbulent structures at its outflow, some provisional inlet conditions have been achieved (but the simulation not ran). This is a pertinent issue to resolve in a future work, namely on the numerical study of the aeolian erosion susceptibility and sensibility to this inflow conditions, which better replicate the naturally-found wind turbulent patterns.

Bibliography

Anderson, John David and J. Wendt. 1995. *Computational Fluid Dynamics*. Vol. 206. Springer.

Ansys. 2016. "Ansys 17.0 - Documentation." Retrieved (https://www.sharcnet.ca/Software/Ansys/17.0/en-us/help/flu_ug/flu_ug_mesh_quality.html).

Argyropoulos, C. D. and N. C. Markatos. 2015. "Recent Advances on the Numerical Modelling of Turbulent Flows." *Applied Mathematical Modelling* 39(2):693–732.

Autodesk. 2019. "Professional-Grade 3D CAD Software for Product Design and Engineering." Retrieved (https://www.autodesk.com/products/inventor/overview).

Bagnold, Ralph Alger. 2012. *The Physics of Blown Sand and Desert Dunes*. Courier Corporation.

Bouffanais, Roland. 2010. "Advances and Challenges of Applied Large-Eddy Simulation." *Computers and Fluids* 39(5):735–38.

Boussinesq, Joseph. 1903. *Thōrie Analytique de La Chaleur Mise En Harmonie Avec La Thermodynamique et Avec La Thōrie Mc̄anique de La Lumi_re: Refroidissement et C̄hauffement Par Rayonnement, Conductibilit⁻des Tiges, Lames et Masses Cristallines, Courants de Convection, Thōrie Mc̄*. Vol. 2. Gauthier-Villars.

Bruno, Luca and Davide Fransos. 2015. "Sand Transverse Dune Aerodynamics: 3D Coherent Flow Structures from a Computational Study." *Journal of Wind Engineering and Industrial Aerodynamics* 147:291–301.

Carneiro, M. V, K. R. Rasmussen, and H. J. Herrmann. 2015. "Bursts in Discontinuous Aeolian Saltation." *Scientific Reports* 5:11109.

Clark, Robert A., Joel H. Ferziger, and William Craig Reynolds. 1979. "Evaluation of Subgrid-Scale Models Using an Accurately Simulated Turbulent Flow." *Journal of Fluid Mechanics* 91(1):1–16.

Courant, Richard, Kurt Friedrichs, and Hans Lewy. 1928. "Über Die Partiellen Differenzengleichungen Der Mathematischen Physik." *Mathematische Annalen* 100(1):32–74.

Elder, Jim. 2006. "Aeolian Dunes and Sandstone: Overview." Retrieved May 4, 2019 (http://smallpond.ca/jim/sand/overview/).

Faria, Raquel, Almerindo D. Ferreira, A. M. G. Lopes, and Antonio C. M. Sousa. 2017. "On the Calibration of Irwin Probes for Flow in Rectangular Ducts with Different Aspect Ratios." *Journal of Fluids Engineering* 139(10):101401.

Faria, Raquel, Almerindo D. Ferreira, João L. Sismeiro, João C. F. Mendes, and Antonio C. M. Sousa. 2011. "Wind Tunnel and Computational Study of the Stoss Slope Effect on the Aeolian Erosion of Transverse Sand Dunes." *Aeolian Research* 3(3):303–14.

Ferreira, Almerindo D. and Maria Rosário M. Fino. 2012. "A Wind Tunnel Study of Wind Erosion and Profile Reshaping of Transverse Sand Piles in Tandem." *Geomorphology* 139–140:230–41.

Ferreira, Almerindo D., Rosário Fino, Thomas Thiis, A. M. G. Lopes, and A. C. .. Sousa. 2018. "On the Modelling of Wind Erosion Threshold of Piles in Tandem." P. 4 in. Korea.

Ferreira, Almerindo D., Sérgio R. Pinheiro, and Sara C. Francisco. 2013. "Experimental and Numerical Study on the Shear Velocity Distribution along One or Two Dunes in Tandem." *Environmental Fluid Mechanics* 13(6):557–70.

Finnigan, J. J. 1988. "Air Flow Over Complex Terrain BT - Flow and Transport in the Natural Environment: Advances and Applications." Pp. 183–229 in, edited by W. L. Steffen and O. T. Denmead. Berlin, Heidelberg: Springer Berlin Heidelberg.

Freitas, Christopher J. 2002. "The Issue of Numerical Uncertainty." *Applied Mathematical Modelling* 26(2):237–48.

Frisch, Uriel and Andreĭ Nikolaevich Kolmogorov. 1995. *Turbulence: The Legacy of AN Kolmogorov*. Cambridge university press.

Germano, Massimo, Ugo Piomelli, Parviz Moin, and William H. Cabot. 1991. "A Dynamic Subgrid-scale Eddy Viscosity Model." *Physics of Fluids A: Fluid Dynamics* 3(7):1760–65.

Gibbs, Jeremy A. 2016a. "LES of Turbulent Flows: Lecture 11." Retrieved (https://gibbs.science/teaching/les/lectures/lecture_11.pdf).

Gibbs, Jeremy A. 2016b. "LES of Turbulent Flows: Lecture 3." 11–15. Retrieved (https://gibbs.science/les/lectures/lecture_03.pdf).

Gibbs, Jeremy A. 2016c. "LES of Turbulent Flows: Lecture 5." Retrieved

(https://gibbs.science/teaching/les/lectures/lecture_05.pdf).

Greeley, Ronald and James D. Iversen. 1987. *Wind as a Geological Process: On Earth, Mars, Venus and Titan*. Vol. 4. CUP Archive.

Greenshields, Christopher J. 2018. *User Guide Version 6*.

Herrmann, H. J., J. S. Andrade, V. Schatz, G. Sauermann, and E. J. R. Parteli. 2005. "Calculation of the Separation Streamlines of Barchans and Transverse Dunes." *Physica A: Statistical Mechanics and Its Applications* 357(1):44–49.

Howard, Alan D. 1977. "Effect of Slope on the Threshold of Motion and Its Application to Orientation of Wind Ripples." *Geological Society of America Bulletin* 88(6):853–56.

Irwin, H. P. A. H. 1981. "A Simple Omnidirectional Sensor for Wind-Tunnel Studies of Pedestrian-Level Winds." *Journal of Wind Engineering and Industrial Aerodynamics* 7(3):219–39.

Issa, Raad I. 1986. "Solution of the Implicitly Discretised Fluid Flow Equations by Operator-Splitting." *Journal of Computational Physics* 62(1):40–65.

Iversen, J. D., James B. Pollack, Ronald Greeley, and Bruce R. White. 1976. "Saltation Threshold on Mars: The Effect of Interparticle Force, Surface Roughness, and Low Atmospheric Density." *Icarus* 29(3):381–93.

Iversen, James D. and Rasmussen, Keld R. 1994. "The Effect of Surface Slope on Saltation Threshold." *Sedimentology* 41(4):721–28.

Iversen, James D. and Bruce R. White. 1982. "Saltation Threshold on Earth, Mars and Venus." *Sedimentology* 29(1):111–19.

Karimi, M., G. Akdogan, K. H. Dellimore, and S. M. Bradshaw. 2012. "Quantification of Numerical Uncertainty in Computational Fluid Dynamics Modelling of Hydrocyclones." *Computers & Chemical Engineering* 43:45–54.

Kolmogorov, Andrey Nikolaevich. 1941. "The Local Structure of Turbulence in Incompressible Viscous Fluid for Very Large Reynolds Numbers." *Cr Acad. Sci. URSS* 30:301–5.

Leonard, A. 1975. "Energy Cascade in Large-Eddy Simulations of Turbulent Fluid Flows." Pp. 237–48 in *Advances in geophysics*. Vol. 18. Elsevier.

Lindblad, Daniel. 2014. "Implementation and Run-Time Mesh Refinement for the k-w SST DES Turbulence Model When Applied to Airfoils."

Liu, Benli, Jianjun Qu, Weimin Zhang, and Guangqiang Qian. 2011. "Numerical

Simulation of Wind Flow over Transverse and Pyramid Dunes." *Journal of Wind Engineering and Industrial Aerodynamics* 99(8):879–88.

Liu, F. 2016. "A Thorough Description of How Wall Functions Are Implemented in OpenFOAM." *Proceedings of CFD with OpenSource Software* 1–33.

Loring, Burlen, Homa Karimabadi, and Vadim Rortershteyn. 2014. *A Screen Space GPGPU Surface LIC Algorithm for Distributed Memory Data Parallel Sort Last Rendering Infrastructures*. Lawrence Berkeley National Lab.(LBNL), Berkeley, CA (United States).

Lund, T. S. 2003. "The Use of Explicit Filters in Large Eddy Simulation." *Computers & Mathematics with Applications* 46(4):603–16.

Markatos, N. C. 1986. "The Mathematical Modelling of Turbulent Flows." *Applied Mathematical Modelling* 10(3):190–220.

Meneveau, Charles. 2010. "Turbulence: Subgrid-Scale Modelling." Retrieved (http://www.scholarpedia.org/article/Turbulence:_Subgrid-Scale_Modeling).

Menter, Florian and Thomas Esch. 2001. "Elements of Industrial Heat Transfer Predictions." P. 650 in *16th Brazilian Congress of Mechanical Engineering (COBEM)*. Vol. 109. sn.

Menter, Florian R., Martin Kuntz, and Robin Langtry. 2003. "Ten Years of Industrial Experience with the SST Turbulence Model." *Turbulence, Heat and Mass Transfer* 4(1):625–32.

Menter, Florian R. 1993. "Zonal Two Equation Kw Turbulence Models for Aerodynamic Flows." P. 2906 in *23rd fluid dynamics, plasmadynamics, and lasers conference.*

Montorfano, Andrea, Federico Piscaglia, and Giancarlo Ferrari. 2013. "Inlet Boundary Conditions for Incompressible Les: A Comparative Study." *Mathematical and Computer Modelling* 57(7–8):1640–47.

Moukalled, F., L. Mangani, and M. Darwish. 2016. *The Finite Volume Method in Computational Fluid Dynamics*. Vol. 113.

Navier, CLMH. 1823. "Mémoire Sur Les Lois Du Mouvement Des Fluides." *Mémoires de l'Académie Royale Des Sciences de l'Institut de France* 6(1823):389–440.

Nicoud, Franck and Frédéric Ducros. 1999. "Subgrid-Scale Stress Modelling Based on the Square of the Velocity Gradient Tensor." *Flow, Turbulence and Combustion* 62(3):183–200.

NPARC. 2008. "Examining Spatial (Grid) Convergence." Retrieved (https://www.grc.nasa.gov/www/wind/valid/tutorial/spatconv.html).

NSERL. 2009. "Wind Erosion."

Oliveira, Luis Adriano and António Gameiro Lopes. 2016. *Mecânica Dos Fluídos, 5. a Edição*.

OpenFOAM Foundation Ltd. 2018. "OpenFOAM Version 6."

Patankar, S. V. and D. B. Spalding. 1972. "A Calculation Procedure for Heat, Mass and Momentum Transfer in Three-Dimensional Parabolic Flows." *Int. J. of Heat and Mass Transfer* 15(10):1787–1806.

Phillips, Mike. 1980. "A Force Balance Model for Particle Entrainment into a Fluid Stream." *Journal of Physics D: Applied Physics* 13(2):221.

Piomelli, Ugo. 1999. "Large-Eddy Simulation: Achievements and Challenges." *Progress in Aerospace Sciences* 35(4):335–62.

Reynolds, William C. 1990. "The Potential and Limitations of Direct and Large Eddy Simulations." Pp. 313–43 in *Whither turbulence? Turbulence at the crossroads*. Springer.

Richardson, Lewis Fry. 1911. "IX. The Approximate Arithmetical Solution by Finite Differences of Physical Problems Involving Differential Equations, with an Application to the Stresses in a Masonry Dam." *Philosophical Transactions of the Royal Society of London. Series A, Containing Papers of a Mathematical or Physical Character* 210(459–470):307–57.

Roache, Patrick J. 1994. "Perspective: A Method for Uniform Reporting of Grid Refinement Studies." *Journal of Fluids Engineering* 116(3):405–13.

Sagaut, Pierre. 2006. *Large Eddy Simulation for Incompressible Flows: An Introduction*. Springer Science & Business Media.

Salim, Salim M. and S. Cheah. 2009. "Wall Y Strategy for Dealing with Wall-Bounded Turbulent Flows." Pp. 2165–70 in *Proceedings of the international multiconference of engineers and computer scientists*. Vol. 2. Citeseer.

Schatz, Volker and Hans J. Herrmann. 2006. "Flow Separation in the Lee Side of Transverse Dunes: A Numerical Investigation." *Geomorphology* 81(1):207–16.

Shao, Yaping and Hua Lu. 2000. "A Simple Expression for Wind Erosion Threshold Friction Velocity." *Journal of Geophysical Research: Atmospheres* 105(D17):22437–

43.

Shur, M., P. R. Spalart, M. Strelets, and A. Travin. 1999. "Detached-Eddy Simulation of an Airfoil at High Angle of Attack." Pp. 669–78 in *Engineering Turbulence Modelling and Experiments 4*. Elsevier.

Smagorinsky, Joseph. 1963. "General Circulation Experiments with the Primitive Equations: I. The Basic Experiment." *Monthly Weather Review* 91(3):99–164.

Spalart, Philippe R. 1997. "Comments on the Feasibility of LES for Wings, and on a Hybrid RANS/LES Approach." in *Proceedings of first AFOSR international conference on DNS/LES*. Greyden Press.

Spalart, Philippe R. 2009. "Detached-Eddy Simulation." *Annual Review of Fluid Mechanics* 41:181–202.

Stokes, G. G. 1845. "On the Theories of the Internal Friction of Fluids in Motion, and of the Equilibrium and Motion of Pendulums." *Trans. Camb. Phil. Soc*.

Sweet, M. L. and Kocurek, G. 1990. "An Empirical Model of Aeolian Dune Lee-Face Airflow." *Sedimentology* 37(6):1023–38.

Tennekes, Hendrik, John Leask Lumley, and J L Lumley. 1972. *A First Course in Turbulence*. MIT press.

Travin, Andrei, Michael Shur, Michael Strelets, and Philippe Spalart. 2000. "Detached-Eddy Simulations Past a Circular Cylinder." *Flow, Turbulence and Combustion* 63(1–4):293–313.

Versteeg, Henk Kaarle and Weeratunge Malalasekera. 2007. *An Introduction to Computational Fluid Dynamics: The Finite Volume Method*. Pearson education.

White, Bruce R. 1996. "Laboratory Simulation of Aeolian Sand Transport and Physical Modelling." *Annals of Arid Zone* 35(3):187–213.

Wiggs, Giles F. S., Ian Livingstone, and Andrew Warren. 1996. "The Role of Streamline Curvature in Sand Dune Dynamics: Evidence from Field and Wind Tunnel Measurements." *Geomorphology* 17(1–3):29–46.

Wilcox, David C. 1988. "Reassessment of the Scale-Determining Equation for Advanced Turbulence Models." *AIAA Journal* 26(11):1299–1310.

Woelke, Michał. 2007. "Eddy Viscosity Turbulence Models Emploed by Computational Fluid Dynamic." *Prace Instytutu Lotnictwa* 92–113.

Yoshizawa, Akira. 1986. "Statistical Theory for Compressible Turbulent Shear Flows, with

the Application to Subgrid Modeling." *The Physics of Fluids* 29(7):2152–64.

Zhiyin, Yang. 2015. "Large-Eddy Simulation: Past, Present and the Future." *Chinese Journal of Aeronautics* 28(1):11–24.

Annex A – Derivation of Bagnold´s threshold equation

Modelling a resting sand grain as an undeformable sphere with a diameter d, the $u_{*t0}(d)$ expression can be derived considering the balance of forces acting on the particle, which lays on a horizontal granular bed under the influence of an airstream. The formula is derived at the instant of entrainment, obtained by the summation of the induced moments about the pivot point (P), as seen in Figure A1. The forces in play are the aerodynamic drag (F_d), the aerodynamic lift (F_l), the net particle weight (F_g) and the interparticle cohesive force (F_i).
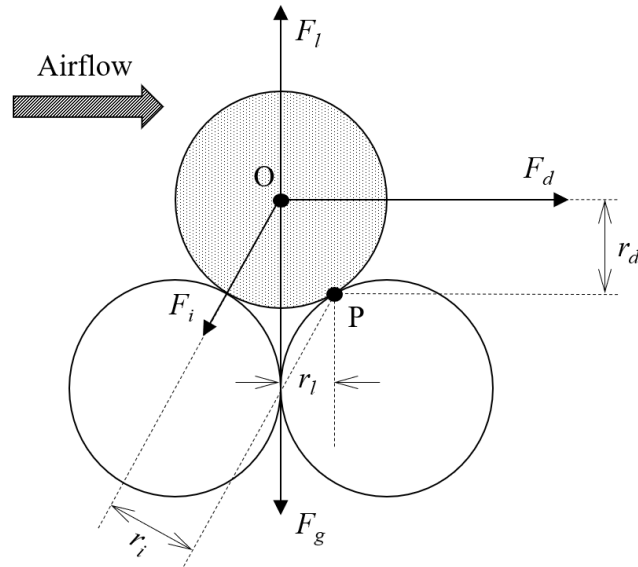
Figure A1. Forces acting on a particle resting a horizontal surface and respective moment arms.

At the onset of particle motion (*i.e.* entrainment instant), the combined driving forces (F_l and F_d) overcome the combined retarding effect (F_g and F_i) and the particle tends to pivot about point P, in the downstream direction. Bagnold (1941) delivers a simple theory for $u_{*t0}(d)$ by solely considering the balance between F_g and F_d.

Let the moment arm lengths of these two forces (r_g and r_d, respectively) be linearly proportional to the particle size (d) and expressed as (Shao and Lu, 2000):

$$r_g = a_g d \tag{A.1}$$

$$r_d = a_d d \tag{A.2}$$

Assuming that the a constants are comparable, $i.e.$ $r_g \approx r_d$, the balance reduces to:

$$a_d F_d = a_g F_g \Leftrightarrow \boxed{F_d \approx F_g}$$ (A.3)

The so-called net particle weigh modulus (F_g) is calculated by means of Equation (A.4). As visible in Figure A1, the sand grain is immersed in air, thus buoyance forces are accounted and deduced from the gross weight. In that expression, ρ_s and ρ are the particle and air densities, correspondingly, and g the gravitational acceleration modulus.

$$F_g = (\rho_s - \rho)\frac{\pi d^3}{6}g$$ (A.4)

Traditionally, the F_d magnitude is expressed as Equation (A.5), but Shao and Lu (2000) argue that the aerodynamic drag coefficient (C_d) is unclear and the precise flow speed at a reference point (U) is uncertain in such strong shear flows. The variable A_c is the particle cross-section perpendicular to the flow. Alternatively, the literature instead relates F_d to u_*, as seen in Equation (A.6), where K_d is a function of the particle friction Reynolds number ($Re_* = u_* d/v$).

$$F_d = \frac{1}{2}C_d \rho A_c U^2$$ (A.5)

$$F_d = K_d \rho d^2 (u_*)^2$$ (A.6)

Substituting in Equation (A.3):

$$(\rho_s - \rho)\frac{\pi d^3}{6}g = K_d \rho d^2 (u_*)^2 \Leftrightarrow u_* = \sqrt{\frac{\pi(\rho_s - \rho)gd}{6K_d \rho}}$$ (A.7)

The Bagnold´s threshold parameter (A), or dimensionless friction velocity threshold, can be defined as in Equation (A.8) (Bagnold, 1941).

$$A = A(Re_{u_{*_t}}) = \sqrt{\frac{\pi}{6K_d}} \in [0.1, 0.2]$$ (A.8)

Finally, one derives the friction velocity threshold for aeolian particles resting on horizontal surfaces (whose prevailing diameter exceeds 100 μm).

$$\boxed{u_{*t0} = A\sqrt{\frac{(\rho_s - \rho)}{\rho}gd}}$$ (A.9)

Annex B – Filtering the conservation equations

From the fully compressible form of the conservation equations (mass and linear momentum), the corresponding incompressible counterparts are derived. The filtering operation is applied to the latter equation system, arriving at the Equations (3.17) and (3.18).

Starting with the equation for the conservation of mass:

$$\frac{\partial \rho}{\partial t} + \frac{\partial (\rho u_i)}{\partial x_i} = 0 \tag{B.1}$$

Applying the incompressibility condition, that is, the density of the fluid in a parcel is constant in time and space ($\rho = \rho_0$) and dividing by ρ_0, one arrives at the conservation of mass differential equation for incompressible flows:

$$\frac{\partial u_i}{\partial x_i} = 0 \tag{B.2}$$

For the conservation of momentum, the complete equation is described as:

$$\frac{\partial (\rho u_i)}{\partial t} + \frac{\partial (\rho u_i u_j)}{\partial x_j} = -\frac{\partial p}{\partial x_i} + \frac{\partial}{\partial x_j}\left[2\mu S_{ij} - \frac{2}{3}\mu \delta_{ij} \frac{\partial u_i}{\partial x_i}\right] + F_i \tag{B.3}$$

In the former expression, F_i represents the field forces acting on the fluid element and the tensors S_{ij} and δ_{ij} describe the strain rate tensor and Kronecker delta, given by:

$$S_{ij} = \frac{1}{2}\left(\frac{\partial u_i}{\partial x_j} + \frac{\partial u_j}{\partial x_i}\right) \tag{B.4}$$

$$\delta_{ij} = \begin{cases} 1 & \text{if } i = j; \\ 0 & \text{if } i \neq j, \end{cases} \tag{B.5}$$

Again, applying the incompressibility condition and dividing by ρ_0, bearing in mind the relation $v = \mu/\rho_0$:

$$\frac{\partial u_i}{\partial t} + \frac{\partial (u_i u_j)}{\partial x_j} = -\frac{1}{\rho_0}\frac{\partial p}{\partial x_i} + v\frac{\partial}{\partial x_j}\left[\left(\frac{\partial u_i}{\partial x_j} + \frac{\partial u_j}{\partial x_i}\right) - \frac{2}{3}\delta_{ij}\frac{\partial u_i}{\partial x_i}\right] + f_i \tag{B.6}$$

Note that the incompressible mass conservation equation appears in the right member, eliminating the respective term. Rearranging and reapplying the continuity equation:

$$\frac{\partial u_i}{\partial t} + \frac{\partial (u_i u_j)}{\partial x_j} = -\frac{1}{\rho_0}\frac{\partial p}{\partial x_i} + \nu\frac{\partial^2 u_i}{\partial x_j^2} + \nu\frac{\partial}{\partial x_i}\left(\frac{\partial u_j}{\partial x_j}\right) + f_i \qquad (B.7)$$

One arrives at the conservation of momentum differential equation for incompressible flows (the subscript "0" is abandoned for the sake of clarity):

$$\frac{\partial u_i}{\partial t} + \frac{\partial (u_i u_j)}{\partial x_j} = -\frac{1}{\rho}\frac{\partial p}{\partial x_i} + \nu\frac{\partial^2 u_i}{\partial x_j^2} + f_i \qquad (B.8)$$

Recalling the filtering properties listed in Table 3.1, the filter operator is applied to Equations (B.2) and (B.8). For the continuity equation the operation resumes to:

$$\widetilde{\frac{\partial u_i}{\partial x_i}} = 0 \Leftrightarrow \frac{\widetilde{\partial u_i}}{\partial x_i} = \tilde{0} \Leftrightarrow \boxed{\frac{\partial \tilde{u}_i}{\partial x_i} = 0} \qquad (B.9)$$

For the Navier-Stokes equation, the filtering operation results in (neglecting field forces):

$$\begin{aligned}
& \overline{\frac{\partial u_i}{\partial t} + \frac{\partial (u_i u_j)}{\partial x_j}} = -\frac{1}{\rho}\frac{\partial p}{\partial x_i} + \nu\frac{\partial^2 u_i}{\partial x_j^2} \\
\Leftrightarrow & \frac{\widetilde{\partial u_i}}{\partial t} + \frac{\widetilde{\partial (u_i u_j)}}{\partial x_j} = -\frac{\widetilde{1}}{\rho}\frac{\partial p}{\partial x_i} + \nu\frac{\widetilde{\partial^2 u_i}}{\partial x_j^2} \\
\Leftrightarrow & \frac{\partial \tilde{u}_i}{\partial t} + \frac{\partial (\widetilde{u_i u_j})}{\partial x_j} = -\frac{1}{\rho}\frac{\partial \tilde{p}}{\partial x_i} + \nu\frac{\partial^2 \tilde{u}_i}{\partial x_j^2}
\end{aligned} \qquad (B.10)$$

A problem arises, as $\widetilde{u_i u_j}$ is the filtered product of two non-filtered variables, and one must decompose the same term, *e.g.* the Leonard (1975) decomposition, where τ_{ij} is the unknow SGS stress tensor, which must be modelled to achieved mathematical closure.

$$\widetilde{u_i u_j} = \tilde{u}_i \tilde{u}_j + \tau_{ij} \qquad (B.11)$$

Finally, the explicit LES-employed, filtered Navier-Stokes equations:

$$\boxed{\frac{\partial \tilde{u}_i}{\partial t} + \frac{\partial (\tilde{u}_i \tilde{u}_j)}{\partial x_j} = -\frac{1}{\rho}\frac{\partial \tilde{p}}{\partial x_i} + \nu\frac{\partial^2 \tilde{u}_i}{\partial x_j^2} - \frac{\partial}{\partial x_j}\left(\tau_{ij}\right)} \qquad (B.12)$$

Appendix A – Boundary conditions dictionaries

```
/*--------------------------------*- C++ -*----------------------------------*\
  =========                 |
  \\      /  F ield         | OpenFOAM: The Open Source CFD Toolbox
   \\    /   O peration     | Website:  https://openfoam.org
    \\  /    A nd           | Version:  6
     \\/     M anipulation  |
\*---------------------------------------------------------------------------*/
FoamFile
{
    version     2.0;
    format      ascii;
    class       volScalarField;
    location    "0";
    object      k; //Turbulence Kinematic Energy (TKE) dictionary
}
// * * * * * * * * * * * * * * * * * * * * * * * * * * * * * * * * * * * * * //

dimensions      [0 2 -2 0 0 0 0]; //m²s⁻²;

internalField   uniform 1.03335; //Freestream TKE – Equation (4.5) (initial value);

boundaryField

{
    inlet
    {
        type            fixedProfile;
        profile         csvFile;
        profileCoeffs
        {
            nHeaderLine     0;
            refColumn       0;
            componentColumns List<label> 1(1);
            separator       ",";
            mergeSeparators 0;
            file            "0/kProfile.csv";
        }
        direction       (0 0 1);
        origin          0;
    }
    outlet
    {
        type            zeroGradient;
    }
    lowerWall
    {
        type            fixedValue;
        value           uniform 1e-10; //Wall-value TKE (tends to zero);
    }
    top
    {
        type            symmetryPlane;
    }
    front
    {
        type            symmetry;
    }
    back
    {
        type            symmetry;
    }
    tandemPiles
    {
        type            fixedValue;
        value           uniform 1e-10; //Wall-value TKE (tends to zero);
    }
}
// ************************************************************************* //
```

```
/*--------------------------------*- C++ -*----------------------------------*\
  =========                 |
  \\      /  F ield         | OpenFOAM: The Open Source CFD Toolbox
   \\    /   O peration     | Website:  https://openfoam.org
    \\  /    A nd           | Version:  6
     \\/     M anipulation  |
\*---------------------------------------------------------------------------*/
FoamFile
{
    version     2.0;
    format      ascii;
    class       volVectorField;
    location    "0";
    object      U; //Velocity field dictionary
}
// * * * * * * * * * * * * * * * * * * * * * * * * * * * * * * * * * * * * * * //
dimensions      [0 1 -1 0 0 0 0]; //m¹s⁻¹

internalField   uniform (8.3 0 0); //Freestream Velocity (initial value);

boundaryField

{
    inlet
    {
        type            fixedProfile; //Power-law of Equation (2.2);
        profile         csvFile;
        profileCoeffs
        {
            nHeaderLine     0;
            refColumn       0;
            componentColumns List<label> 3(1 2 3);
            separator       ",";
            mergeSeparators 0;
            file            "0/UProfile.csv";
        }
        direction       (0 0 1);
        origin          0;
    }
    outlet
    {
        type            zeroGradient;
    }
    lowerWall
    {
        type            noSlip;
    }
    top
    {
        type            symmetryPlane;
    }
    front
    {
        type            symmetry;
    }
    back
    {
        type            symmetry;
    }
    tandemPiles
    {
        type            noSlip;
    }
}
// ************************************************************************* //
```

```
/*--------------------------------*- C++ -*----------------------------------*\
  =========                 |
  \\      /  F ield         | OpenFOAM: The Open Source CFD Toolbox
   \\    /   O peration     | Website:  https://openfoam.org
    \\  /    A nd           | Version:  6
     \\/     M anipulation  |
\*---------------------------------------------------------------------------*/
FoamFile
{
    version     2.0;
    format      ascii;
    class       volScalarField;
    location    "0";
    object      omega; //Specific TKE dissipation rate dictionary
}
// * * * * * * * * * * * * * * * * * * * * * * * * * * * * * * * * * * * * * //

dimensions      [0 0 -1 0 0 0 0]; //s⁻¹;

internalField   uniform 16.9423; // Freestream Omega – Equation (4.3) (initial value);

boundaryField

{
    inlet
    {
        type            fixedProfile;
        profile         csvFile;
        profileCoeffs
        {
            nHeaderLine    0;
            refColumn      0;
            componentColumns List<label> 1(1);
            separator       ",";
            mergeSeparators 0;
            file            "0/wProfile.csv";
        }
        direction       (0 0 1);
        origin          0;
    }
    outlet
    {
        type            zeroGradient;
    }
    lowerWall
    {
        type            omegaWallFunction; //Valid for any yPlus;
        value           uniform 8.3102e+06; // Near-wall Omega – Equation (4.4);
    }
    top
    {
        type            symmetryPlane;
    }
    front
    {
        type            symmetry;
    }
    back
    {
        type            symmetry;
    }
    tandemPiles
    {
        type            omegaWallFunction; //Valid for any yPlus;
        value           uniform 8.3102e+06; // Near-wall Omega – Equation (4.4);
    }
}

// ************************************************************************* //
```

```
/*--------------------------------*- C++ -*----------------------------------*\
  =========                 |
  \\      /  F ield         | OpenFOAM: The Open Source CFD Toolbox
   \\    /   O peration     | Website:  https://openfoam.org
    \\  /    A nd           | Version:  6
     \\/     M anipulation  |
\*---------------------------------------------------------------------------*/
FoamFile
{
    version     2.0;
    format      ascii;
    class       volScalarField;
    location    "0";
    object      p; //Kinematic pressure dictionary
}
// * * * * * * * * * * * * * * * * * * * * * * * * * * * * * * * * * * * * * * //

dimensions      [0 2 -2 0 0 0 0]; //m²s⁻² (kinematic pressure);

internalField   uniform 0; (initial value);

boundaryField
{
    inlet
    {
        type            zeroGradient;
    }
    outlet
    {
        type            fixedValue;
        value           uniform 0;
    }
    lowerWall
    {
        type            zeroGradient;
    }
    top
    {
        type            symmetryPlane;
    }
    front
    {
        type            symmetry;
    }
    back
    {
        type            symmetry;
    }
    tandemPiles
    {
        type            zeroGradient;
    }
}


// ************************************************************************* //
```

```
/*--------------------------------*- C++ -*----------------------------------*\
  =========                 |
  \\      /  F ield         | OpenFOAM: The Open Source CFD Toolbox
   \\    /   O peration     | Website:  https://openfoam.org
    \\  /    A nd           | Version:  6
     \\/     M anipulation  |
\*---------------------------------------------------------------------------*/
FoamFile
{
    version     2.0;
    format      ascii;
    class       volScalarField;
    location    "0";
    object      nut; //Eddy-viscosity dictionary
}
// * * * * * * * * * * * * * * * * * * * * * * * * * * * * * * * * * * * * * //

dimensions      [0 2 -1 0 0 0 0]; //m²s⁻¹;

internalField   uniform 0; (initial value);

boundaryField
{
    inlet
    {
        type            calculated; //Computed by k and Omega;
        value           uniform 0;
    }
    outlet
    {
        type            calculated; //Computed by k and Omega;
        value           uniform 0;
    }
    lowerWall
    {
        type            nutLowReWallFunction; //Mandatory to any Low-Re model (as kOmegaSST);
        Cmu             0.09;
        kappa           0.41;
        E               9.8;
        value           uniform 0;
    }
    top
    {
        type            symmetryPlane;
    }
    front
    {
        type            symmetry;
    }
    back
    {
        type            symmetry;
    }
    tandemPiles
    {
        type            nutLowReWallFunction; //Mandatory to any Low-Re model (as kOmegaSST);
        Cmu             0.09;
        kappa           0.41;
        E               9.8;
        value           uniform 0;
    }
}


// ************************************************************************* //
```